ADVANCING EARTH AND SPACE SCIENCES

JGR Atmospheres

RESEARCH ARTICLE
10.1029/2023JD038622

Special Section:
Southern Ocean clouds, aerosols, precipitation and radiation

Key Points:

- A strong relationship between drop clustering and entrainment-mixing exists on large spatial scales (0.1–1.0 km)
- Drop clustering is positively correlated with large ice (maximum dimension exceeding 300 μm) number concentrations in mixed phase clouds

Correspondence to:
J. J. D'Alessandro,
johndal@uw.edu

Citation:
D'Alessandro, J. J., & McFarquhar, G. M. (2023). Impacts of drop clustering and entrainment-mixing on mixed phase shallow cloud properties over the Southern Ocean: Results from SOCRATES. *Journal of Geophysical Research: Atmospheres*, *128*, e2023JD038622. https://doi.org/10.1029/2023JD038622

Received 3 FEB 2023
Accepted 20 MAY 2023

Impacts of Drop Clustering and Entrainment-Mixing on Mixed Phase Shallow Cloud Properties Over the Southern Ocean: Results From SOCRATES

John J. D'Alessandro[1,2,3] and Greg M. McFarquhar[1,2]

[1]Cooperative Institute for Severe and High Impact Weather Research and Operations, University of Oklahoma, Norman, OK, USA, [2]School of Meteorology, University of Oklahoma, Norman, OK, USA, [3]Now at Department of Atmospheric Sciences, University of Washington, Seattle, WA, USA

Abstract Entrainment and associated mixing (i.e., entrainment-mixing) have been shown to impact drop size distributions. However, most past studies have focused on warm clouds and have not considered the impacts on mixed phase clouds (i.e., those containing liquid and ice particles). This study characterizes the impacts of entrainment-mixing on mixed phase cloud properties over the Southern Ocean using in situ observations. By taking advantage of strong correlations between droplet clustering and entrainment-mixing, a clustering metric is used as a proxy to assess the degree of mixing. This maximizes the available sample size for a statistical analysis of entrainment-mixing impacts on mixed phase properties. A positive relationship is found between the magnitude of droplet clustering and large ice concentrations (those with maximum dimensions greater than ~300 μm), suggesting entrainment-mixing enhances the Wegener-Bergeron-Findeisen (WBF) process. Particle size distributions are averaged over different ranges of liquid (liquid water content (LWC)) to total water content (TWC) ratio. Since the ratio is expected to transition from 1 to 0 during glaciation, differences in the distributions provide insight into the relation of entrainment-mixing to mixed phase cloud evolution. Mixed phase samples with the greatest large ice concentrations occur at LWC/TWC < 0.4 in low clustering regions. However, these samples are relatively few, whereas high clustering regions have a greater frequency of samples with LWC/TWC < 0.4. This suggests sublimation/vapor sinks associated with entrainment can counteract the enhanced WBF. In high clustering regions, distributions of small droplets are relatively constant and large droplets (>30 μm) are preferentially removed as LWC/TWC transitions from 1 to 0.

Plain Language Summary Mixed phase clouds (i.e., liquid and ice particles within the same sample volume) have been notoriously difficult to represent in weather and climate models. To improve simulations, continued exploration of mixed phase properties and processes using high resolution observations is necessary. This study uses in situ observations to explore the potential impacts of entrainment and the associated mixing (i.e., entrainment-mixing) on mixed phase microphysical properties. In situ observations are taken primarily from low-level clouds over the Southern Ocean acquired during the Southern Ocean Cloud-Radiation Aerosol Transport Experimental Study. This study takes advantage of the fact that cloud drop clustering is strongly correlated with entrainment-mixing. Namely, drop clustering is used as a proxy variable to diagnose entrainment-mixing and the associated impacts on mixed phase clouds. Results suggest entrainment-mixing can result in an enhanced Wegener-Bergeron-Findeisen (WBF) process, as seen by a positive relationship between drop clustering and large ice concentrations. However, the enhanced WBF process can be offset by sufficiently strong entrainment-mixing.

1. Introduction

Mixed phase clouds, where liquid and ice particles occur in the same sample volume, have been observed in maritime and continental regions ranging from the tropics to the poles (e.g., Cossich et al., 2021; Costa et al., 2017; Hogan et al., 2003; Korolev et al., 2003; McFarquhar et al., 2007; Mioche et al., 2015; A. E. Morrison et al., 2011; Wang et al., 2021), and can be associated with cloud types ranging from thin stratiform layers to deep convective clouds (Korolev et al., 2017). The common occurrence and even persistence (H. Morrison et al., 2012) of mixed phase clouds is unexpected due to differences in the saturation vapor pressure of liquid and ice. When liquid and ice particles are present, ice should grow at the expense of liquid drops, commonly known as the Wegener-Bergeron-Findeisen (WBF) process (Bergeron, 1928; Findeisen, 1938; Wegener, 1911).

Mixed phase clouds are ubiquitous over the Southern Ocean (D'Alessandro et al., 2019, 2021; Huang et al., 2012, 2021; Mace et al., 2021; A. E. Morrison et al., 2011; Schima et al., 2022). Large errors in simulated shortwave radiative flux common for climate models over this region has been attributed to the incorrect representation of mixed phase clouds, and primarily to an underrepresentation of supercooled liquid (Bodas-Salcedo et al., 2016; Naud et al., 2014). However, recent model updates approximately capture and likely overestimate observed supercooled liquid frequencies (Gettelman et al., 2020; Yang et al., 2021). In addition, climate models often over-estimate the WBF, resulting in unrealistic glaciation rates (Tan & Storelvmo, 2016). Correctly simulating mixed phase clouds is crucial toward improving both weather and climate models because of their impact on precipitation (Mülmenstädt et al., 2015) and radiation (Sun & Shine, 1994).

Previous theoretical and modeling studies considered the impacts of turbulent mixing on mixed phase properties. For example, Korolev and Mazin (2003) found that liquid could persist within a vertically oscillating mixed phase air parcel and that liquid could form within an ice cloud when the vertical velocity exceeds a critical threshold. These findings are consistent with those from Hill et al. (2014) using a large-eddy simulation model and from Heymsfield (1977) using doppler radar and airborne measurements. Less work has explored impacts of entrainment-mixing on mixed phase properties, although one recent study (Hoffmann, 2020) utilized a millimeter resolution linear eddy model to show that entrainment can enhance the WBF process due to increased droplet evaporation if it is not offset by the spatial inhomogeneity of phase within the mixed areas.

Cloud top entrainment is important to quantify as it controls the evolution of macro- and microscale features of low-level clouds. Entrainment rates are directly related to vertical gradients of temperature, humidity and radiative cooling directly overlying the cloud (Houze, 2014; Mellado, 2017). When considering the impacts of entrainment-mixing on microphysical properties, it is common to characterize mixing events as homogenous or inhomogeneous (M. B. Baker et al., 1980; Latham & Reed, 1977) as these two alternative mixing schemes result in different pathways for the evolution of drop size distributions. Homogeneous mixing is associated with vigorous mixing of dry air into cloudy regions, resulting in all droplets undergoing at least partial evaporation. Inhomogeneous mixing is associated with weaker mixing. As dry air is slowly mixed within the cloud, a few drops will be preferentially evaporated to return the entrained area to near saturation. Inhomogeneous mixing typically has a greater impact on drop concentrations than on sizes. In contrast, homogeneous mixing has a greater impact on average drop sizes since all droplets are at least partly evaporated. The former is associated with drop size distributions having decreasing concentrations at all sizes, whereas the latter is often characterized by a shift of the distribution toward smaller sizes.

The Damköhler number (Damköhler, 1940) is commonly used to characterize the type of mixing and to determine the impact of entrainment on cloud microphysical properties (Dimotakis, 2005). It is defined as

$$\mathrm{Da} = \frac{\tau_m}{\tau_r}, \tag{1}$$

where τ_m is the turbulent mixing time (i.e., eddy turnover time) and τ_r is the response time of the microphysical properties to mixing. When the response time of the cloud particles is much slower than the mixing time, Da << 1, this indicates homogenous mixing. In contrast, cloud particles rapidly reacting to weak entrainment events result in Da >> 1 which indicates extreme inhomogeneous mixing. The τ_m is expressed as

$$\tau_m = \left(L^2/\varepsilon\right)^{\frac{1}{3}} \tag{2}$$

where L is the length scale of the entrained eddy (i.e., dry air) and ε is the turbulent dissipation rate. Calculations of τ_r vary depending on whether the evaporation time (τ_{evap}), phase relaxation time (τ_{phase}), or reaction time (τ_{react}) is chosen, as each expression is associated with different assumptions. Thus, τ_r is more ambiguous than τ_m (e.g., Z. Gao et al., 2018; Lu et al., 2018). Further discussion of homogeneous and inhomogeneous mixing can be found in Devenish et al. (2012) and Korolev et al. (2016).

Although a considerable amount of work has characterized mixing in warm clouds, often examining drop size broadening and the potential for rain initiation (e.g., Grabowski & Wang, 2013; Jensen & Baker, 1989; Lasher-Trapp et al., 2005; Tölle & Krueger, 2014), little such work has been done for mixed phase clouds. This study provides an observational evaluation of entrainment-mixing impacts on mixed phase cloud properties. The remainder of the paper is organized as follows. Section 2 describes the instrumentation used and relevant analysis techniques. Section 3 evaluates the relationship between drop clustering and multiple measures of entrainment-mixing, which forms the basis of using clustering as a proxy to broadly diagnose the intensity of entrainment-mixing. Section 4 relates clustering to mixed phase cloud properties to assess the impacts of mixing. The last two sections (Sections 5 and 6) include additional discussion and concluding remarks.

2. Instrumentation

This study uses observations acquired with instruments onboard the National Science Foundation/National Center for Atmospheric Research Gulfstream-V (GV) aircraft during the Southern Ocean Cloud-Radiation Aerosol Transport Experimental Study (SOCRATES). SOCRATES was based out of Hobart, Tasmania and consisted of 15 research flights from 15 January to 28 February 2018. The aircraft sampled the Southern Ocean from 42° to 62°S and from 133° to 163°W, primarily targeting cold sector boundary layer clouds. The portions of flights returning north toward Hobart primarily consisted of 10-min level legs above cloud, in cloud, and below cloud, followed by sawtooth legs to obtain vertical profiles of cloud properties. Both stratiform and cumuliform clouds were sampled by the aircraft. Additional information on flight objectives and analyses can be found in McFarquhar et al. (2021).

A suite of cloud probes and other instrumentation was installed on the GV. The cloud droplet probe (CDP) is a single-scatter particle probe which gives information of cloud PSDs for particles with maximum dimension (hereafter referred to as D) ranging from 2 to 50 μm. The two-dimensional stereo probe (2DS) is an optical imaging array probe with two photodiode arrays having resolutions of 10 μm from which PSD information is derived. Although the width of the photodiode array of the 2DS corresponds to particles with maximum dimensions ranging from 10 to 1,280 μm, only particles having D greater than or equal to 50 μm were included in the derived PSDs because of its small and highly uncertain depth of field for D < 50 μm (e.g., Baumgardner & Korolev, 1997). The SOCRATES 2DS particle morphological data and size distribution information (Wu & McFarquhar, 2019) were determined using the University of Illinois/Oklahoma Optical Probe Processing Software (UIOOPS; McFarquhar et al., 2017, 2018), and include corrections for the removal of shattered artifacts (Field et al., 2003, 2006). Particles larger than the width of the photodiode array were reconstructed given the particle center is within the array (Heymsfield & Parrish, 1978). Mass distribution functions were determined from habit-dependent mass-size relationships following Jackson et al. (2012, 2014) for the different particle habits identified in UIOOPS (McFarquhar et al., 2018) following a modified Holroyd (1987) approach.

Samples are determined to be in-cloud or clear-sky following D'Alessandro et al. (2021), utilizing measurements from the CDP and 2DS. Samples are considered in-cloud if the derived mass content of CDP observations (M_{CDP}) is greater than 10^{-3} g m^{-3} or if any particles with D > 50 μm were detected by the 2DS. The small threshold of M_{CDP} ensures that even very tenuous clouds are included in the sample. The phase of in-cloud samples is determined following D'Alessandro et al. (2021), which determines the phase of small cloud particles (D < 50 μm) using a set of threshold values for the CDP and Rosemount Icing Detector measurements, whereas the phase of large particles (D > 50 μm) is determined using multinomial logistic regression as well as visual examination of particle imagery from the 2DS. Modifications to the scheme developed by Schima et al. (2022) affected the identified phase for only 2% of the times and did not impact the findings of this study; hence, the original D'Alessandro et al. (2021) phases are used in this analysis. Only time periods identified as liquid or mixed phase are used here. Number concentrations of the CDP (N_{CDP}) greater than 10 cm^{-3} have generally been found to be liquid samples in the past (e.g., D'Alessandro et al., 2021; Finlon et al., 2019; Heymsfield et al., 2011; Lance et al., 2010), and N_{CDP} as low as 1 cm^{-3} are generally found to be liquid samples from previous analysis of SOCRATES observations (D'Alessandro et al., 2021). Analysis in this study is restricted to samples with $N_{CDP} > 5$ cm^{-3}, which are assumed to represent liquid droplets.

The phase of a 2DS sample can be classified as either liquid, ice or mixed. Since all CDP observations are liquid for the periods used in this study, a cloud sample is considered mixed phase if the 2DS is classified as mixed or ice phase. Cloud PSDs combine CDP and 2DS size distributions, corresponding to cloud particles less than and greater than 50 μm, respectively. When the 2DS sample is ice phase, liquid bulk properties are derived from the CDP and ice bulk properties are derived from all 2DS particles. For 2DS mixed phase samples, liquid bulk properties are derived from the CDP and from 2DS particles identified as spherical, whereas bulk properties of ice are derived from non-spherical all 2DS particles. Because ice particles can appear spherical due to variations in particle orientation and shape, previous studies have often applied

10.1029/2023JD038622

additional conditions for determining the phase of spherical particles (e.g., Cober & Isaac, 2012). Following Schima et al. (2022), mixed phase samples must have the ratio of round particles having D > 100 μm to all particles with D > 100 μm greater than 0.3 to apply the bulk properties as described. Otherwise, all particles greater than 100 μm are classified as ice. Particles from 50 to 100 μm are classified as ice or liquid if they are non-spherical or spherical, respectively.

Additional instrumentation includes the Rosemount temperature probe. For steady conditions, the estimated accuracy and precision are 0.3 and 0.01 K, respectively. Wind components were measured using the Radome Gust Probe in combination with pitot tubes and the differential Global Positioning System. Cooper et al. (2016) reports a net uncertainty in the standard measurements of the horizontal wind components of 0.4 m s^{-1} and the uncertainty in vertical wind measurements of 0.12 m s^{-1}, although these thresholds apply to ideal sampling conditions only. Additional information on the GV gust probe performance and processing is provided in the manager's report (Earth Observing Laboratory, 2018). Water vapor measurements are obtained from a 25 Hz Vertical Cavity Surface Emitting Laser (VCSEL) hygrometer (Zondlo et al., 2010). Additional laboratory calibrations of the VCSEL water vapor measurements were conducted in summer 2018, and the final data were reprocessed (Diao, 2021). Relative humidity (RH) is calculated following Murphy and Koop (2005). The combined uncertainties from temperature and water vapor measurements results in the uncertainty of RH ranging from 6.3% to 6.7%. Temperature, RH and wind components of the ambient air are used to determine Da in Section 3.1.

3. Entrainment-Mixing and Clustering Calculations

To calculate τ_m, ε is determined using equations 11 and 12 from Meischner et al. (2001), which utilizes work from Paluch and Baumgardner (1989) and Panofsky and Dutton (1984). The calculation of L follows S. Gao et al. (2021), namely

$$\mathrm{L} = \mathrm{F} \times \mathrm{TAS}/f \tag{3}$$

where TAS is true air speed of the aircraft, f is the sampling frequency and F is the fraction of clear-sky observations within each 1 Hz sample, determined using 10 Hz observations. Clear-sky samples in S. Gao et al. (2021) were defined as droplet free, whereas a less stringent definition of derived mass content less than 10^{-3} g m^{-3} is applied here (D'Alessandro et al., 2021). The calculations of τ_r for the liquid and mixed phase follow Pinsky et al. (2018), where both expressions are phase relaxation times expressing the time for reaching equilibrium conditions between the condensate and vapor content (Appendix A). These expressions of τ_r are inversely proportional to the particle mean radius and number concentrations.

Two clustering metrics are used in this study. The clustering index (CI) is a commonly used metric to quantify cloud droplet clustering, whose application in cloud microphysics was first introduced in B. A. Baker (1992). CI is defined as

$$\mathrm{CI} = \frac{\sigma^2}{\overline{x}} - 1, \tag{4}$$

which takes account of the fact that a uniform Poisson distribution has the variance (σ^2) equal to the mean ($\overline{x}$) of a given quantity. Thus, CI equals zero for a perfectly homogeneous distribution and increases from this value with increasing heterogeneity (whereas values less than zero are characteristically underdispersed). A potential caveat of CI is its inherent volume dependence, where CI contains "memory" of varying spatial scales within the sample volume (further discussed in Shaw et al. (2002)). The volume average pairwise correlation (VAPC) is introduced to partially offset this dependence and reduce scale memory,

$$\mathrm{VAPC} = \frac{1}{\overline{x}}\left(\frac{\sigma^2}{\overline{x}} - 1\right) = \frac{1}{\overline{x}}(\mathrm{CI}) \tag{5}$$

where CI is weighted by the average quantity. To scale the results logarithmically, an altered CI (ACI) is introduced as

$$\mathrm{ACI} = \log_{10}\left(\frac{\sigma^2}{\overline{x}}\right), \tag{6}$$

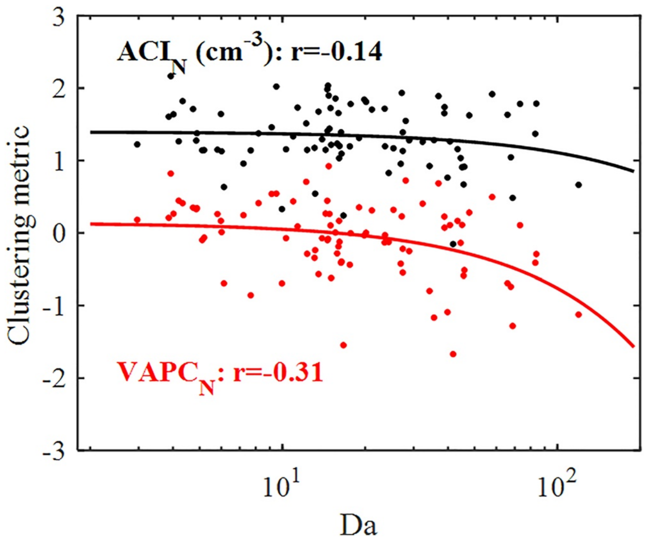

Figure 1. The clustering metrics ACI_N (black markers) and $AVAPC_N$ (red markers) versus Damköhler number. Results are shown for 1 Hz observations at all cloud tops as determined in D'Alessandro et al. (2023), where cloud top is defined as z_n greater than 0.975. Respective correlations are shown in the plot. Note that only samples with clear-sky fraction (F) greater than 0 are included in the plot (otherwise Da = 0).

where the subtraction of one is removed so results are always greater than 0. Log scaling CI improves the visualization of clustering results, which will be evident in the following section. Similarly, an altered VAPC (AVAPC) is introduced as

$$\text{AVAPC} = \log_{10}\left(\frac{\sigma^2}{\bar{x}^2}\right) = \log_{10}\left(\frac{1}{\bar{x}}(\text{CI}+1)\right). \tag{7}$$

For this study, 10 Hz observations are used to determine ACI and AVAPC at 1 Hz resolution. Clustering results are applied to N_{CDP} (ACI_N and $AVAPC_N$; similar to D'Alessandro et al. (2023)).

3.1. Droplet Clustering as a Proxy for Mixing

Analysis in the following section shows that applying a clustering method on a relatively coarse spatial scale (~100 m) can give a direct, qualitative description of the degree of mixing. Higher values of cloud drop clustering indices have commonly been observed at cloud edges previously (e.g., Beals et al., 2015; Dodson & Small Griswold, 2019; Small & Chuang, 2008), including for Southern Ocean clouds (D'Alessandro et al., 2023). Clustering can be related to localized turbulent flows, where droplets cluster in low vorticity regions (Shaw et al., 1998).

Figure 1 shows the relationship between the clustering metrics and Da at cloud top. Following D'Alessandro et al. (2023), cloud top samples are identified as those in-cloud data from ascending and descending flight legs where the normalized cloud height (z_n) exceeds 0.975, with z_n determined following McFarquhar et al. (2007) as

$$z_n = \frac{(z - z_{\text{cloud\_base}})}{(z_{\text{cloud\_top}} - z_{\text{cloud\_base}})} \tag{8}$$

where z refers to altitude, and $z_{\text{cloud\_top}}$ and $z_{\text{cloud\_base}}$ refer to the altitudes of cloud top and cloud base for a particular layer, respectively. D'Alessandro et al. (2023) determines $z_{\text{cloud\_base}}$ and $z_{\text{cloud\_top}}$ as the lowest and highest in-cloud sample of a given cloud layer, respectively. Although the decrease of $AVAPC_N$ with Da is more pronounced than for ACI_N, both clustering metrics are negatively correlated with Da. This is analogous to clustering being positively correlated with mixing strength (i.e., low Da), which is expected as drop clustering is shown as strongly correlated to entrainment-mixing further in this section. Additionally, all samples having Da > 1 is consistent with most prior studies commonly observing inhomogeneous rather than homogeneous mixing (e.g., Andrejczuk et al., 2009; Beals et al., 2015; Burnet & Brenguier, 2007; S. Gao et al., 2021; Jia et al., 2019), especially at the relatively large mixing length scales used here (Burnet & Brenguier, 2007; Kumar et al., 2018; Lehmann et al., 2009). This finding is also consistent with Sanchez et al. (2020), who had to assume extreme inhomogeneous mixing in parcel model simulations of single-layer clouds from SOCRATES to obtain results consistent with drop concentrations reported by the CDP. However, the relationship between ACI_N and Da in Figure 1 is quite weak. In fact, previous studies have used other mixing measures in conjunction with Da to characterize mixing due to a wide range of observed Da (e.g., Burnet & Brenguier, 2007; Kumar et al., 2014; Lu et al., 2011; Yum et al., 2015). One reason for this is that there is no commonly accepted method for determining the eddy length scale. Further, Lehmann et al. (2009) noted that multiple eddy length scales (and thus mixing time scales) exist for a subsequent entrainment-mixing event. Because of this, they introduced the transition length scale (L*), where values greater (lower) than the measured eddy length scale are indicative of homogeneous (inhomogeneous) mixing. It is defined as

$$\text{L}^* = \varepsilon^{\frac{1}{2}}\,\tau_r^{\frac{3}{2}}, \tag{9}$$

where Lehmann et al. (2009) argue τ_r should use the lower time scale between τ_{phase} and τ_{evap}. Values of L* are determined using the SOCRATES observations. Similar to Lehmann et al. (2009), most values are on the order

10.1029/2023JD038622

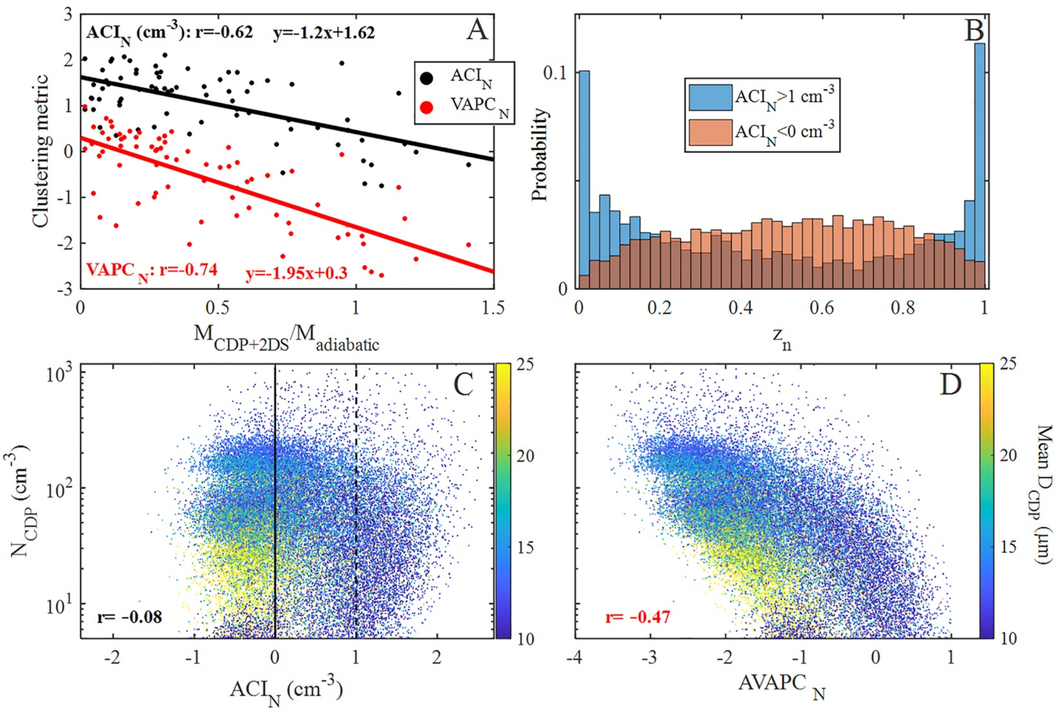

Figure 2. (a) The clustering metrics ACI_N (black markers) and $AVAPC_N$ (red markers) related to the ratio of the actual and adiabatic cloud mass. Results are shown for 1 Hz observations at cloud top similar to Figure 1, but only for single layer clouds with thicknesses greater than 30 m. Unlike Figure 1, results include samples with clear-sky fraction (f) greater than and equal to 0. First order polynomial best fit lines as well as correlations are shown for the respective clustering metrics. (b) Normalized frequency distributions of z_n for different ranges of ACI_N. Unlike (a), z_n is taken from single and multi-layer clouds for all layer thicknesses. Bins for z_n are at 0.025 intervals. (c) ACI_N and (d) $AVAPC_N$ related to N_{CDP}. Results are colored by mean D_{CDP}. The solid and dashed vertical lines in (c) correspond to $ACI_N = 0$ cm^{-3} and $ACI_N = 1$ cm^{-3}, respectively, which are used as threshold values for low and high ACI_N in (b).

of meters and lower, much shorter than the sampling length scales of this study. For liquid phase conditions, τ_{evap} is taken from Rogers and Yau (1996) and for mixed phase conditions, τ_{evap} is replaced by the glaciation time (i.e., time for the total amount of liquid water to convert to ice) taken from Hoffmann (2020).

Other mixing measures often include mixing diagrams relating drop size, mass and number concentrations to their respective adiabatic values. Relating actual to adiabatic properties can give insight to the strength of entrainment-mixing, since adiabatically derived values assume the respective air parcel does not mix with the surrounding environment. In order to evaluate clustering in relation to adiabatically derived quantities, Figure 2a shows the clustering metrics as a function of the ratio of the observed mass content at cloud top ($M_{CDP+2DS}$) over the adiabatic mass content ($M_{adiabatic}$). $M_{adiabatic}$ is determined using pressure, temperature and water vapor measurements at z_{cloud_base} similar to Braun et al. (2018). Both ACI_N (black points) and $AVAPC_N$ (red points) show a strong negative relationship with the adiabatic mass ratio (correlation of −0.62 for ACI_N and −0.74 for AVAPC), showing that the degree of clustering can be directly related to the degree of mixing. It is important to note that the adiabatic assumption applies only to non-precipitating clouds. If removing cloud top data associated with precipitating cloud layers, the inverse correlations increase in magnitude (−0.73 for ACI_N and −0.85 for $AVAPC_N$). Similar to the dependence of CI on Da, a stronger correlation is found for $AVAPC_N$ than for ACI_N. Nevertheless, ACI_N is used to determine the degree of mixing for the duration of the study because ACI_N is less dependent on N_{CDP} ($r = -0.08$) than $AVAPC_N$ ($r = -0.47$). This is seen when comparing the clustering metrics and N_{CDP} in Figures 2c and 2d. The entire range of $AVAPC_N$ shifts toward smaller sizes with increasing N_{CDP}, whereas the range of ACI_N is relatively constant for all N_{CDP}. Results are colored by the number weighted mean diameter (mean D_{CDP}) in Figures 2c and 2d. Distinct modes are seen for mean D_{CDP}. For N_{CDP} greater than 40 cm^{-3}, the mean D_{CDP} varies from 15 to 25 μm and the majority of samples (65%) occur here. For $N_{CDP} < 40$ cm^{-3}, higher mean D_{CDP} (>25 μm) occur at low clustering values and lower mean D_{CDP} (<10 μm) occur at high clustering values. The low mean D_{CDP} and high ACI_N are primarily where $z_n < 0.1$ and $z_n > 0.9$,

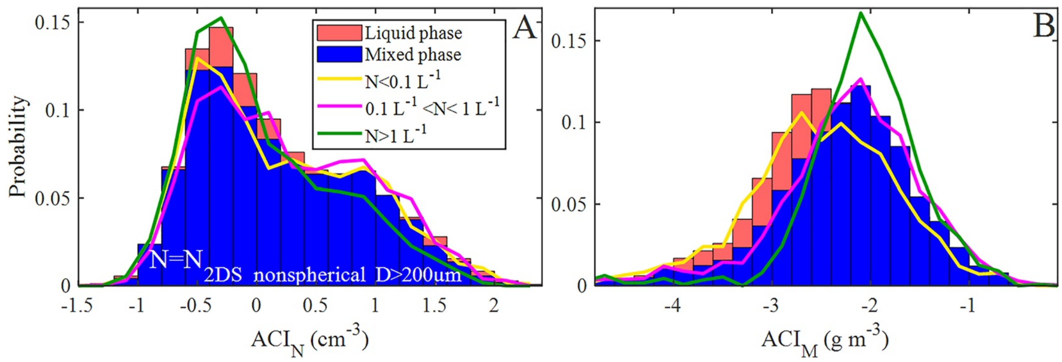

Figure 3. Normalized frequency distributions of (a) ACI_N and (b) ACI_M shown for different cloud phases (shaded colors). The colored lines show normalized frequency distributions for mixed phase results with varying ice concentrations exceeding 200 μm.

which is shown by the normalized frequency distributions of z_n at high ACI_N in Figure 2b (blue bars). In contrast, the high Mean D_{CDP} are primarily within the cloud core as shown by z_n at low ACI_N in Figure 2b (orange bars). These high Mean D_{CDP} are primarily precipitating samples (including drizzle and ice), as 70% of these points detected the presence of particles on the 2DS with D > 200 μm (not shown). Figure 2d shows that similar precipitating samples (i.e., having high mean D_{CDP}) within or near the cloud core are associated with higher $AVAPC_N$ than many non-precipitating samples having low mean D_{CDP} at higher N_{CDP} (e.g., all samples having $AVAPC_N$ below −2.5), since they are weighted by lower values of N_{CDP}. Although ACI_N is used to diagnose mixing, the choice of clustering metric is inconsequential since exchanging ACI_N with $AVAPC_N$ throughout the analyses of this study show similar trends.

Droplet clustering impacts processes such as precipitation initiation (Shaw et al., 1998), evolution of raindrop distributions (McFarquhar, 2004), and ice crystal growth (Castellano et al., 2004, 2008). However, clustering relevant to such mechanisms is associated with spatial scales orders of magnitude smaller (∼1 cm) than that presented here (∼100 m). To determine the direct relationship between the presence of ice and drop clustering, drop clustering in liquid and mixed phase samples is compared. Figure 3a shows normalized frequency distributions of ACI_N for liquid and mixed phase conditions as red and blue shading, respectively. Mixed phase results are separately shown for different ice number concentrations with D > 200 μm. This threshold is chosen due to depth of field uncertainties and insufficient number of photodiodes shadowed for smaller sizes (e.g., Baumgardner et al., 2017). Distributions are relatively similar, although the liquid phase results are slightly more kurtotic and the mixed phase results have a slight peak at 1 cm^{-3}. Distributions for different ice number concentration ranges (yellow, magenta and green lines) are relatively similar to those of liquid and total mixed phase samples. Perhaps unexpectedly, mixed phase conditions with the greatest number of ice particles have distributions most resembling the liquid phase. This is seen using the sum of the absolute difference in the bin values (i.e., Euclidian distance) for the liquid phase and high ice concentration distributions (0.034), compared with the mixed phase and high ice concentration distributions (0.053). Mann-Whitney U-tests and Kolmogorov-Smirnov tests were performed to test the similarity of the distributions for the varying ice concentration ranges. The Whitney-Mann U-test determines whether the median of one distribution is significantly greater or less than the other, whereas the two-sample Kolmogorov-Smirnov test determines the significance of the maximum absolute difference between the two cumulative frequency distributions, both of which use lookup tables. These tests are chosen since they do not require prior knowledge of the distributions' shapes. Results suggest there is no statistically significant difference between the distributions of the two lower ice concentration ranges with the mixed phase distribution, as well as between the highest ice concentration range and the liquid phase distribution. Specifically, both tests do not reject the null hypothesis, namely, that the distributions are similar, at a significance level of 5%.

Normalized frequency distributions of clustering calculated using M_{CDP} (ACI_M) are shown in Figure 3b and test the impact of using ACI_M rather than ACI_N for the mixing analysis. The distribution of ACI_M for mixed phase samples is clearly shifted toward greater values than for the liquid phase, with a mode approximately 1 g m^{-3} greater. Compared with ACI_N, the Euclidian distance between the liquid and mixed phase bin values is a factor of 2 greater (0.09) than ACI_N (0.04). Figure 3b also shows that the ACI_M distributions shift toward higher values

10.1029/2023JD038622

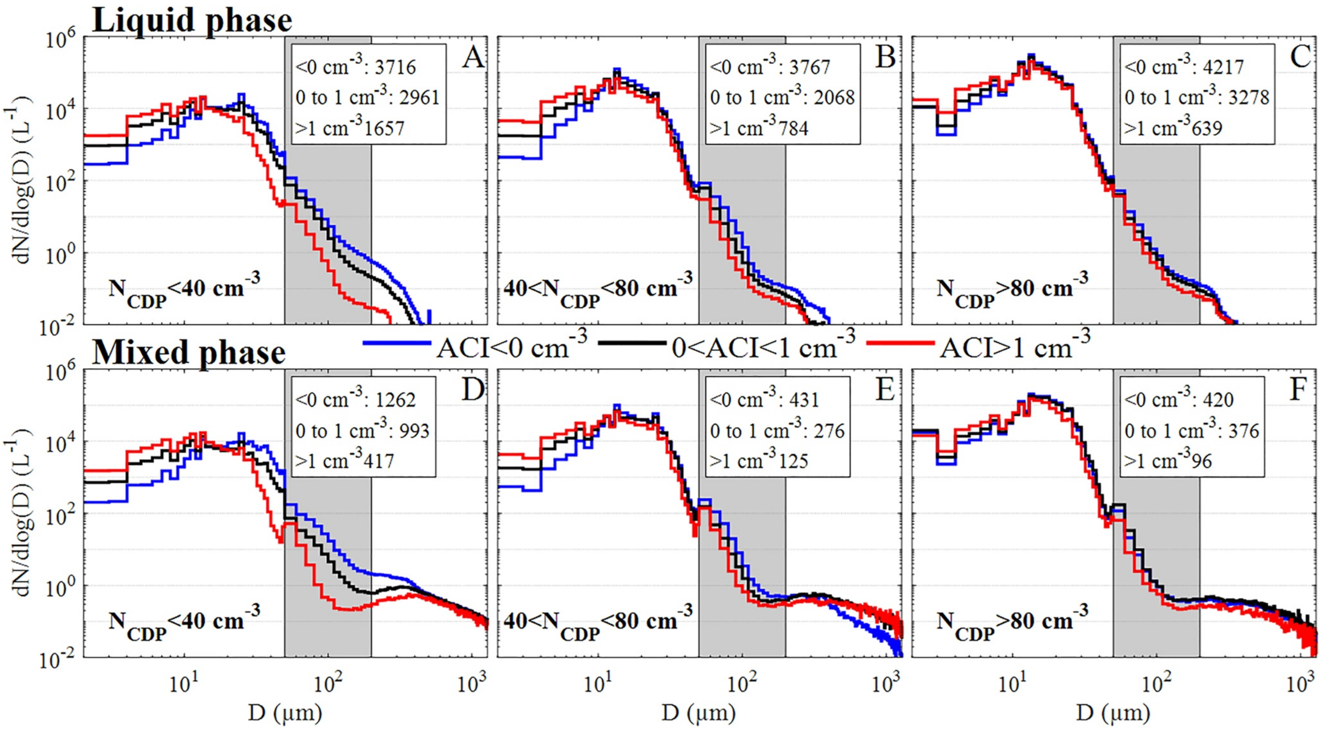

Figure 4. (a–c) Average particle size distributions for the liquid phase and (d–f) mixed phase shown for different ranges of ACI_N by the different colored lines. Results are shown for different ranges of N_{CDP} in the respective columns. The number of samples are shown in the respective panels. Gray shading from 50 to 200 μm represents particle sizes associated with depth of field uncertainties (e.g., Baumgardner et al., 2017).

with increasing ice concentrations. The sum of the Euclidian distances between the mixed phase and all of the different ice concentration ranges for ACI_M is also higher by a factor of 2 (0.20) than for ACI_N (0.11). Since the liquid and mixed phase distributions are more comparable for ACI_N, and no apparent bias associated with ice concentrations is observed for ACI_N, entrainment-mixing is qualitatively determined using drop number rather than drop mass clustering. Further, similarly distributed ACI_N for varying ice concentrations in Figure 3a suggests drop clustering can be used as a proxy variable for diagnosing entrainment-mixing in mixed phase clouds without the concern that ice particles may alternatively impact clustering values.

An initial analysis using ACI_N as a proxy for entrainment-mixing is shown in Figure 4. Particle size distributions (PSDs) are averaged over different ranges of ACI_N for the liquid phase (Figures 4a–4c) and mixed phase (Figures 4d–4f) in order to observe how entrainment-mixing impacts PSDs. PSDs with larger ACI_N should be associated with greater magnitudes of entrainment-mixing. Results are separated into different ranges of N_{CDP}. For both phases, the greatest differences in the PSDs for different ACI_N is seen for N_{CDP} less than 40 cm^{-3} (Figures 3a and 3d), where PSDs are shifted toward smaller sizes with increasing ACI_N. Distributions are most identical at the highest N_{CDP}, which show the greatest deviations at the smallest drop sizes ($D < 7$ μm) for varying ACI_N. This is confirmed by taking the Euclidian distance of the normalized PSDs (i.e., dividing each bin by the sum of the total distribution function), which when summed for the PSDs at $N_{CDP} < 40$ cm^{-3} is a factor of 2.5 greater than for PSDs at $N_{CDP} > 80$ cm^{-3}. This shift is observed for all particle sizes in the liquid phase (1A), but only for particles less than 400 μm in the mixed phase (Figure 4d). Drizzle drops do not likely reach sizes larger than ~400 μm at temperatures less than 0°C due to the potential for aircraft icing. This suggests a resilience of large ice crystals from sublimating, which is consistent with a replenishing water vapor supply from evaporating liquid.

The shift toward smaller sizes with larger ACI_N is consistent with condensate loss due to evaporation and sublimation. Such a shift is characteristically attributed to homogeneous mixing, whereas inhomogeneous mixing typically causes a decrease in the number distribution functions at all particle sizes (i.e., a downward shift in the PSDs) (e.g., Korolev et al., 2016). However, this appearance of homogeneous mixing can be a consequence of combining PSDs from varying environments. For example, when a cloud with average $N_{CDP} > 80$ cm^{-3} has

10.1029/2023JD038622

an entrainment-mixing event that decreases the local drop concentration to less than 40 cm^{-3} it would then be included in the left column. This is consistent with PSDs of $N_{CDP} < 40\ cm^{-3}$ and high ACI_N having high number distribution functions at D < 10 μm, which are more similar to PSDs of $N_{CDP} > 80\ cm^{-3}$ compared with lower ACI_N, assuming larger particle concentrations primarily decrease. Mixed phase results in the following section may suggest this. This is also suggested by high ACI_N number distribution functions of D > 100 μm in $N_{CDP} < 40\ cm^{-3}$ liquid phase samples being the most similar to those at $N_{CDP} > 80\ cm^{-3}$ ($N(\log(D)) < 10^{-1}\ L^{-1}$) compared to lower ACI_N.

To address this potential discrepancy (i.e., the appearance of prevalent homogeneous mixing), results must account for the background cloud and environmental properties. This is done by analyzing results relative to average quantities of cloud transects, which are regions of neighboring samples. Transects are defined by consecutive in-cloud samples having $N_{CDP} > 5\ cm^{-3}$ (similar to D'Alessandro et al., 2021). Transects are split so that (a) the number of 1 Hz observations never exceeds 10 and (b) transect lengths are at least 1 km. For example, a set of 66 neighboring in-cloud samples would be split into six transects having 10 samples and one transect of six samples. If one of the transects has a length less than 1 km, it is discarded. This results in 1781 transects having lengths ranging from 1 to 2.1 km, with 86% of transects having lengths from 1,200 to 1,500 m. Quantities will be prefaced with "average" (e.g., average ACI_N) when referring to transect data, or referenced to by their quartile values (e.g., N_{CDP} > 50th percentile).

The average ACI_N and average $AVAPC_N$ are shown in relation to the N_{CDP} 20th and 80th percentiles for all transects in Figures 5a and 5b, respectively. To provide an all-encompassing analysis of mixing and maximize the sample size, in-cloud data are included in the analysis regardless of their proximity to cloud edge. Both ACI_N and $AVAPC_N$ increase as points diverge from the 1:1 line. This is consistent with greater mixing and the resulting evaporation of available condensate within localized regions of the transects, which are represented by points further from the 1:1 line where the 20th and 80th percentiles of N_{CDP} are more different. Specifically, these clustering values (where the 20th and 80th percentiles of N_{CDP} are more different) are capturing cloud filaments on the order of meters produced by entrainment-mixing events. Figures 5c and 5d shows the covariance of the clustering metrics for the N_{CDP} 20th and 80th percentiles for all transects. The vast majority of values are negative (>85%) and increase in magnitude with greater divergence of the N_{CDP} percentiles. This shows that clustering and N_{CDP} within most transects are negatively correlated (i.e., clustering is primarily correlated to the low N_{CDP} samples rather than high N_{CDP} within the respective transects), consistent with clustering localized to regions of low droplet concentrations resulting from entrainment-mixing processes. Mixing for increasing divergence in the N_{CDP} percentiles is also evident in Figure 5e, which shows points colored by average Mean D_{CDP}. The lowest average Mean D_{CDP} are observed at the greatest differences in the N_{CDP} percentiles, consistent with decreasing drop sizes due to evaporation.

Mixing diagrams relating droplet concentration and volume weighted mean radius (r_v) have commonly been used in the past to distinguish homogeneous from inhomogeneous mixing (e.g., Burnet & Brenguier, 2007; Lehmann et al., 2009; Pawlowska et al., 2000) as homogeneous mixing is associated with greater variability of r_v. This variability is analyzed in Figure 5f, which shows points colored by the difference of the 80th and 20th percentiles of r_v. The difference in r_v percentiles does not increase with increasing difference of N_{CDP} percentiles, but rather with decreasing total N_{CDP} (both 80th and 20th N_{CDP} percentiles decreasing). This irregularity highlights why studies often use complementary measures of mixing alongside N-r_v relationships (e.g., Gerber et al., 2008; Lehmann et al., 2009). Many of these points with low N_{CDP} have the highest average Mean D_{CDP} associated with precipitation (discussed in reference to Figures 2c and 2d). Further, average ACI_N and $AVAPC_N$ are the least similar at low N_{CDP}, where average $AVAPC_N$ are relatively high regardless of the difference in N_{CDP} percentiles. Many of these relatively high values of $AVAPC_N$ overlap with the high Mean D_{CDP} associated with precipitation. In addition, the correlation of clustering with the log-scale difference in the 80th and 20th N_{CDP} percentiles is much greater for ACI_N despite not having results directly weighted by N_{CDP} as for $AVAPC_N$ (shown in Figures 5a and 5b), which is likely due to differences at log average N_{CDP}. These findings highlight the reason for choosing to use average ACI_N for the remaining analysis.

Figure 5 has thus shown that droplet clustering is directly related to differences in the background droplet concentrations. To relate the transects directly to mixing measures, Figure 6 shows average ACI_N related to average L and τ_m. Droplet clustering is significantly correlated with average L ($r = 0.53$), consistent with the negative

10.1029/2023JD038622

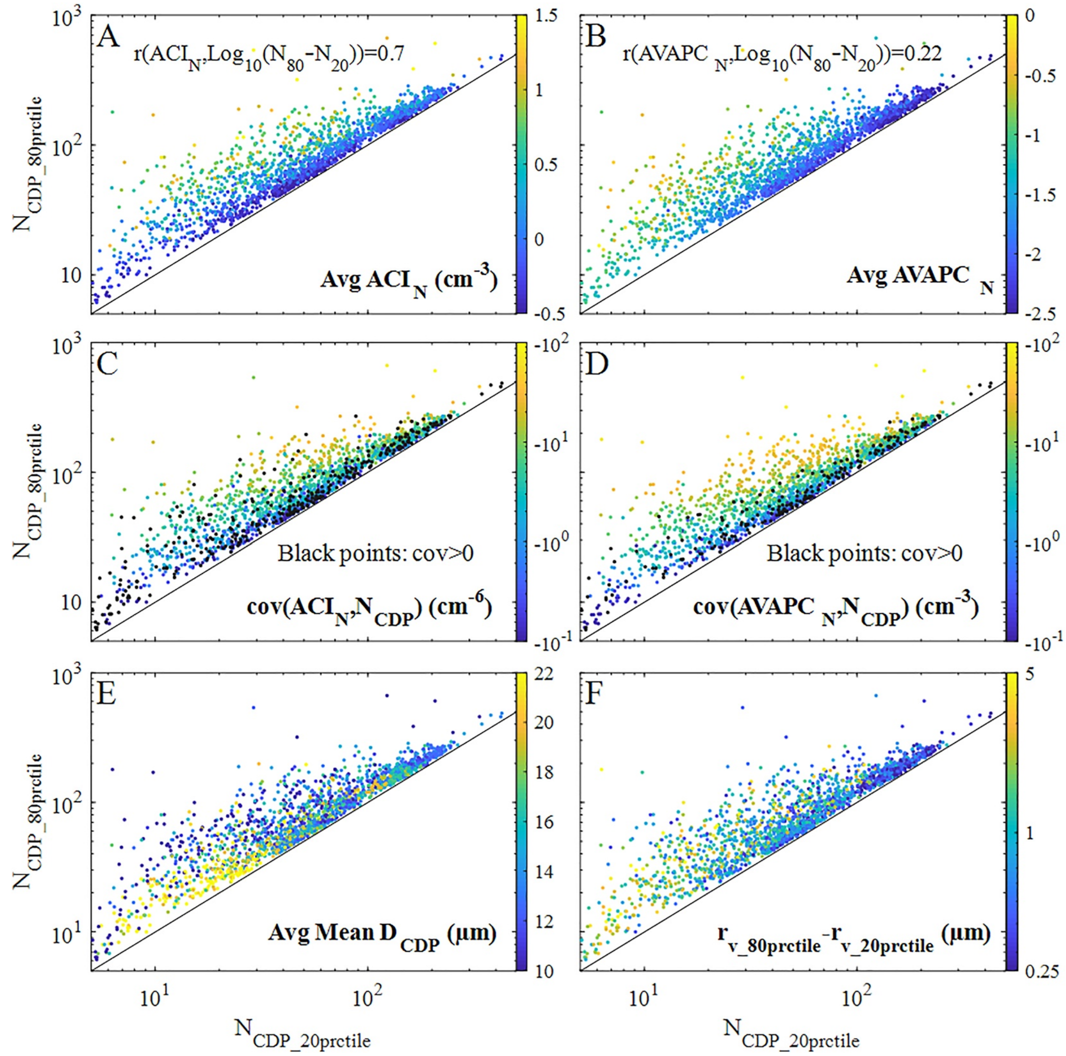

Figure 5. Scatter plots of the 80th percentile N_{CDP} and 20th percentile N_{CDP} for transect data. Results are colored by (a) average ACI_N, (b) average $AVAPC_N$, (c) covariance of ACI_N and N_{CDP}, (d) covariance of $AVAPC_N$ and N_{CDP}, (e) average mean D_{CDP} and (f) the difference of the 80th and 20th percentiles of the volume weighted mean radius. The black line represents the 1:1 line.

covariance of average ACI_N and low N_{CDP} within transects (Figure 5c). Clustering is also positively correlated with τ_m, which considers the instantaneous turbulent motions directly related to ε.

Multiple benefits are associated with utilizing clustering as a proxy variable. It allows for an indirect estimation of L by obtaining an approximation of F without relying on a stringent clear-sky threshold, since clustering is associated with lower number concentrations resulting from evaporation (Figures 5a–5d). This allows for low N_{CDP} gaps between cloud filaments, which may not meet the stringent "droplet-free" condition, to be considered in the mixing analysis. This method also maximizes the total number of available samples. Other methods such as controlling results by the mass content over the adiabatic mass content similarly limits the possible sample size by limiting observations to regions adiabatic values can be derived. This also applies to other metrics such as entrainment rate, which is generally restricted to the entrainment interfacial layer. Further, ambiguous assumptions and uncertainties in determining entrainment rates (Chen et al., 2011; Romps, 2010; Wood, 2012) and Da are avoided. An additional benefit associated with the use of transects is that results are directly applicable to weather models having comparable horizontal grid sizes (∼1 km). The following section presents findings incorporating the use of transects to characterize the impacts of mixing.

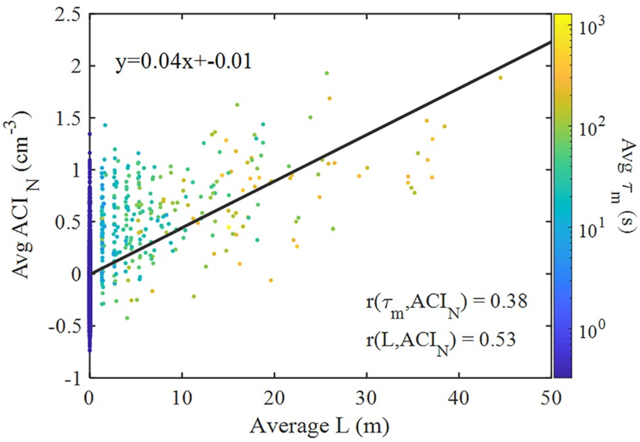

Figure 6. Transect average ACI_N related to the average length scale (L). Results are colored by the average mixing relaxation time (τ_m). Correlations between average ACI_N and the two averaged mixing variables are shown in the panel, as well as a first order polynomial best fit line.

4. Impacts of Mixing

Figure 7 shows average PSDs for liquid phase (Figures 7a–7c) and mixed phase (Figures 7d–7f) samples. Figure 7 differs from Figure 4 in that results are organized by different ranges of 1 Hz ACI_N as well as average ACI_N, with the largest averages in the right column. Transects expected to be associated with stronger entrainment-mixing events are in the right column, whereas weaker or nonexistent entrainment-mixing is associated with the left panels. Percentiles of 1 Hz ACI_N meeting the conditions within each respective panel are shown as the different colored PSDs. The PSDs organized by 1 Hz percentiles are relatively similar within each respective panel, suggesting relative homogeneity amongst 1 Hz ACI_N within transects. However, notable differences are observed between the PSDs within the varying panels. For both phases, higher percentiles of 1 Hz ACI_N (>80th; red lines) generally have lower number distribution functions for D > 50 μm at average ACI_N greater than the 30th percentile compared with lower ACI_N percentiles (black and blue lines; Figures 7b, 7c, 7e, and 7f). For mixed phase samples, this trend is only observed from 50 to 300 μm for average ACI_N 30th to 70th percentiles and from 50 to 200 μm for above

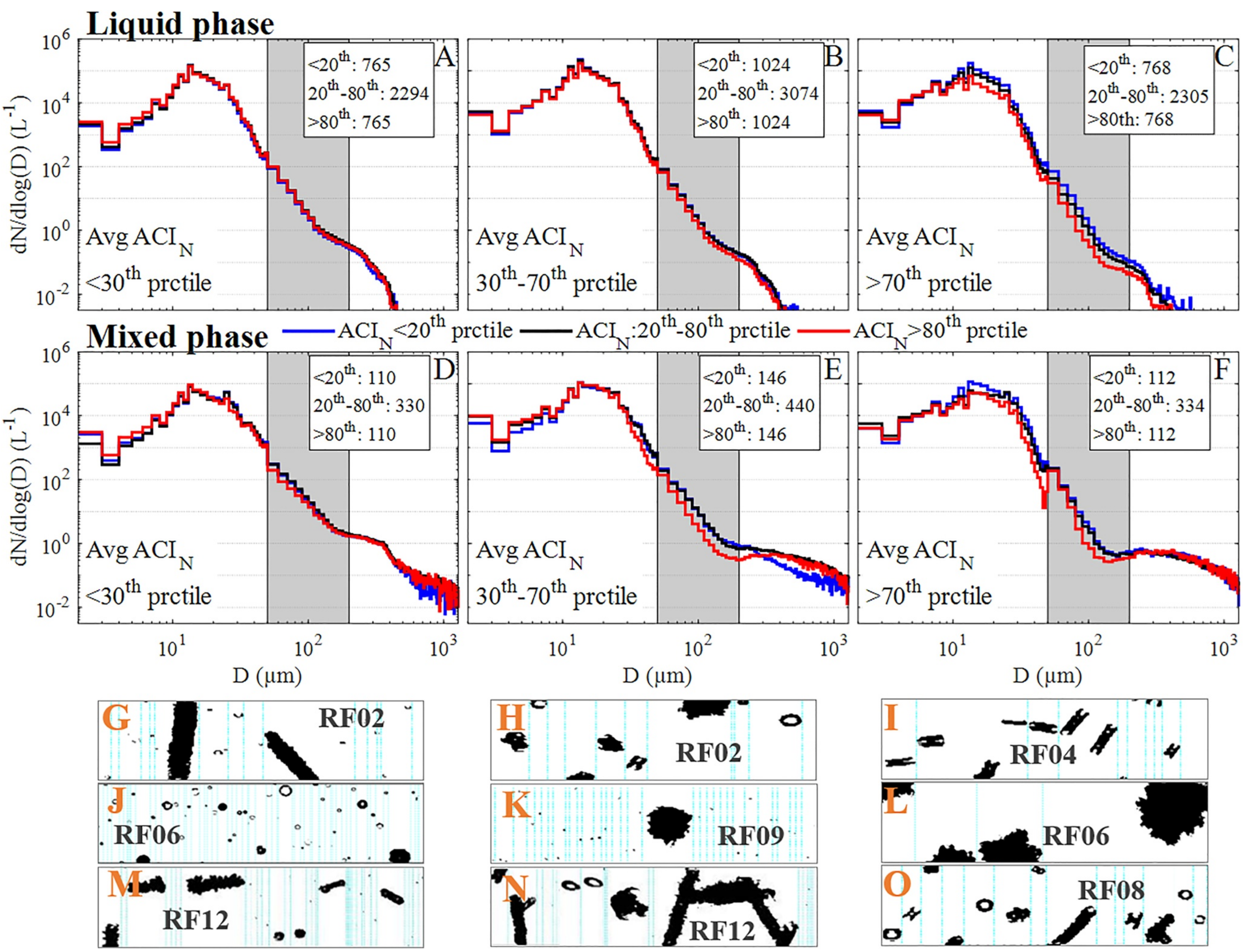

Figure 7. (a–c) Average particle size distributions for liquid and (d–f) mixed phase samples. Results are separated by percentiles of transect average ACI_N for each column. Different colored lines represent varying percentiles of 1 Hz ACI_N associated with the respective transect average ACI_N percentiles. Images underlying each column show representative cases of 2DS cloud particle imagery for the respective average ACI_N percentiles.

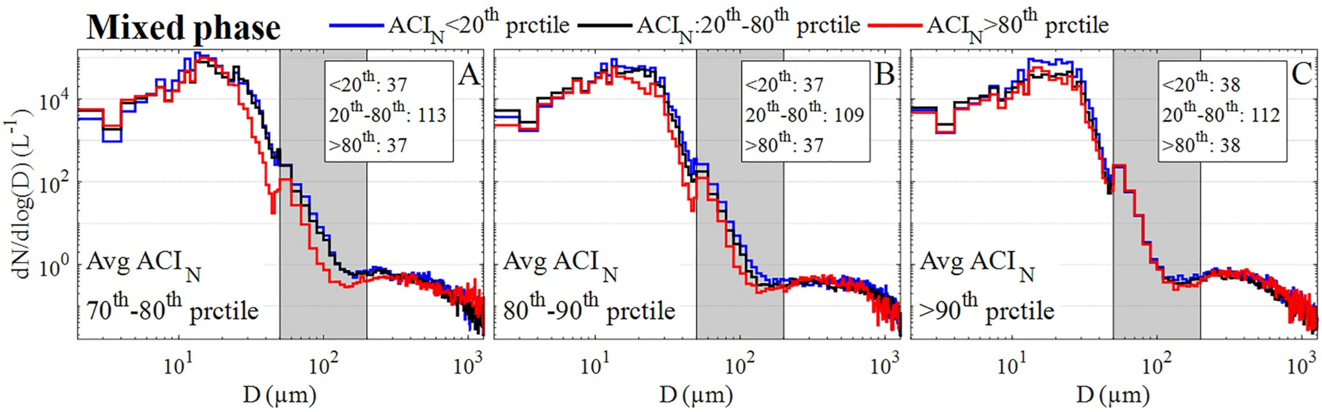

Figure 8. Similar to Figure 7, except results from Figure 7F are separated into three average ACI_N percentile ranges.

the 70th percentile (Figures 7e and 7f). Lower number distribution functions of 1 Hz ACI_N > 80th are also seen from 10 to 50 μm, most notably at average ACI_N greater than 70th percentile. These lower N(log(D)) for greater 1 Hz ACI_N is characteristic of inhomogeneous mixing, which was not evident in Figure 4 when transect data were not used.

The most distinguishing differences of PSDs are observed over different ranges of average ACI_N. For the liquid phase, PSDs are relatively similar amongst the different ranges, with the greatest differences observed at the largest drop sizes. Specifically, at D ∼ 14 μm the number distribution functions are $\sim 10^5$ L^{-1} regardless of average ACI_N, whereas the number distribution functions of large drops (D greater than ∼40 μm) steadily decrease with increasing average ACI_N, consistent with evaporation from entrainment. The PSDs for mixed phase conditions are much more variable amongst average ACI_N compared with the liquid phase. The most notable trend is the difference in the number distribution functions of large particles between average ACI_N less than and greater than the 30th percentile. Less than the 30th percentile, N(log(D)) from ∼100 to 400 μm are observed at 1–10 L^{-1}, and rapidly decrease to 0.1 L^{-1} and lower at sizes greater than 600 μm (Figure 7d). This peak is primarily attributed to samples from mixed phase drizzle associated with the second and sixth research flights (RF02&06, respectively). Representative particle imagery for the different ranges of average ACI_N are shown underlying the respective columns, and the cases shown for RF02 and RF06 highlight these drizzle cases within the lower average ACI_N transects. Drizzle from RF02 occurred together with large ice crystals as seen in Figure 7g, whereas drizzle from RF06 occurred mainly in the absence of ice with the exception of a few cases of small graupel, seen as the aspherical particles in Figure 7j. Number distribution functions from ∼400 to 800 μm increase with increasing average ACI_N (>30th percentile) by a factor of 3–5. Additionally, 1 Hz ACI_N from the 30th to 70th average ACI_N percentiles (Figure 7e) capture this transition, namely, N(log(D)) at D > 400 μm increase above the 20th percentile, and a "dip" occurs between ∼100 and 200 μm. This dip is shown below to be likely related to the removal of large drops. The increase in number distribution functions from ∼400 to 800 μm with increasing average ACI_N as well as the 1 Hz ACI_N in Figure 7e is consistent with enhanced WBF due to droplet evaporation, as noted by Hoffmann (2020) (i.e., increasing concentrations of large ice particles).

Strong mixing events are further examined in Figure 8, where mixed phase results greater than the 70th percentile are separated into 70th–80th (Figure 8a), 80th–90th (Figure 8b), and greater than 90th (Figure 8c) percentiles. Although there is no clear average ACI_N threshold that categorically defines the presence of entrainment-mixing, the right-most panel with the highest ACI_N in Figure 8 shows the clearest downward shifts in PSDs amongst 1 Hz ACI_N percentiles (expected with inhomogeneous mixing; Figure 7f). This adds confidence toward relating the strength of entrainment-mixing to mixed phase properties. Number distribution functions for D greater than 300 μm increase with increasing average ACI_N. Most notably, number distribution functions slightly increase from 300 to 500 μm with increasing average ACI_N. Specifically, N(log(D)) vary from 0.3 to 0.8 L^{-1} (0.2–0.5 L^{-1}) above (below) the 90th percentile of average ACI_N, suggesting large ice concentrations increase with more prominent entrainment-mixing. In addition, mixed phase PSDs have less prominent peaks at ∼15 μm and a slight broadening from 15 to 25 μm with increasing average ACI_N, which although observed in Figures 7d–7f is more pronounced here. Overall, drop number distribution functions for D < 10 μm are relatively similar when compared

10.1029/2023JD038622

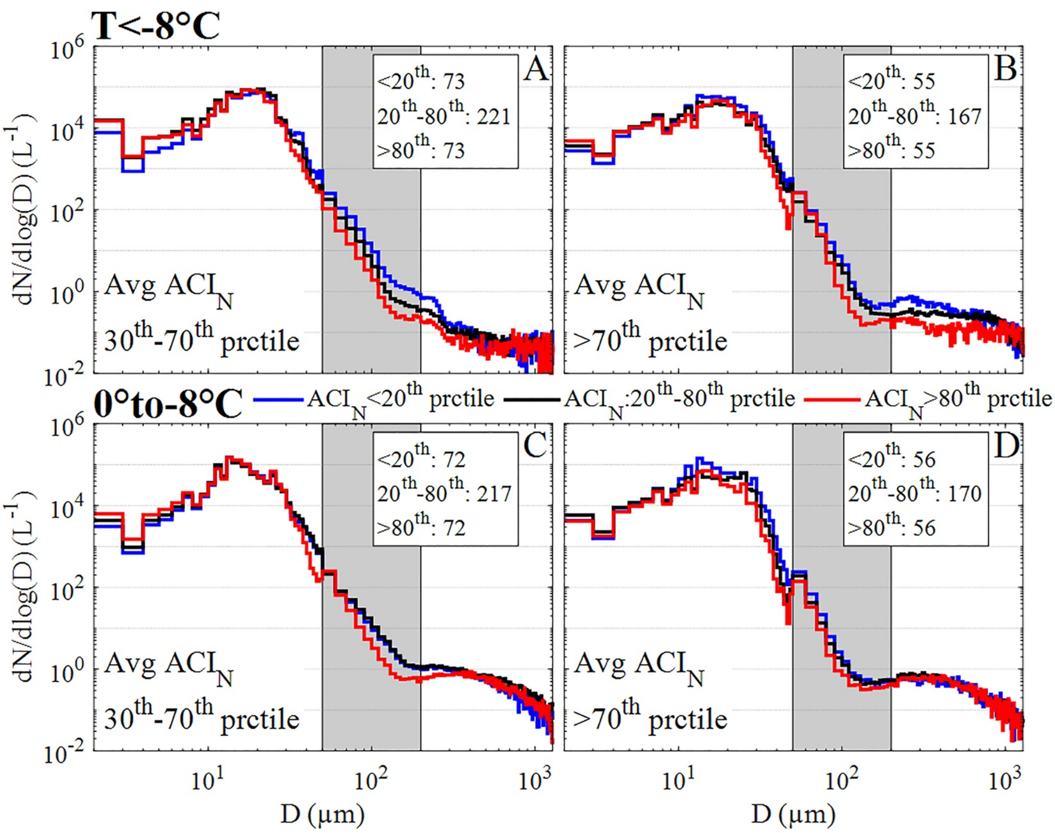

Figure 9. Similar to Figure 7, except results are only shown for mixed phase at temperatures (a and b) less than −8°C and (c and d) greater than −8°C.

amongst the average ACI_N percentiles, whereas relatively larger drops may be preferentially evaporating, as seen by an approximate order of magnitude decrease in number distribution functions at 50 μm with increasing ACI_N.

To evaluate how results vary for different temperatures, mixed phase results for average ACI_N greater than the 30th percentile are separated into different temperature ranges in Figure 9, with lower (higher) temperatures at A&B (C&D). Similar to Figure 7, downward shifts of PSDs for greater 1 Hz ACI_N percentiles at larger average ACI_N (indicative of inhomogeneous mixing) are observed for both temperature ranges. Number distribution functions for D > 400 μm are relatively similar for varying 1 Hz ACI_N at temperatures greater than −8°C, which may suggest weak mixing is sufficient to induce an enhanced WBF process. This is consistent with increased N(log(D)) at D > 400 μm for average ACI_N above the 30th percentile (Figures 7d and 7e). It may also suggest an enhanced WBF process is more prevalent at lower temperatures, where the difference between the liquid and ice saturation vapor pressures is greater. This is consistent with number distribution functions at temperatures less than −8°C, outside the Hallett-Mossop secondary ice crystal production zone (Hallett & Mossop, 1974), which markedly increase for average ACI_N greater than the 70th percentile.

Findings of the increasing number distribution functions of large ice with increasing average ACI_N have thus far been attributed to entrainment-mixing events enhancing WBF. Considering that the characteristic pathway of the WBF process is the transition of liquid to ice, the liquid water content (LWC) over the total water content (TWC; ice and liquid) would be expected to transition from 1 to 0 during these events. Thus, if an enhanced WBF process were present, a hypothetical set of mixed phase samples would more likely be associated with lower values of LWC/TWC compared to a weak WBF process. Figure 10 directly relates average ACI_N to 1 Hz mixed phase samples within the transects for all temperatures (Figure 10a), temperatures less than −8°C (Figure 10b) and temperatures greater than −8°C (Figure 10c). The joint histogram is normalized over each average ACI_N bin. For all temperatures, the frequency of LWC/TWC at 0.9–1.0 gradually decreases from ~0.9 to 0.2 as average ACI_N increases from −0.6 to 1.0. The frequency of lower LWC/TWC correspondingly increases with increasing average ACI_N as well, having frequencies skewed toward higher LWC/TWC at low average ACI_N and more

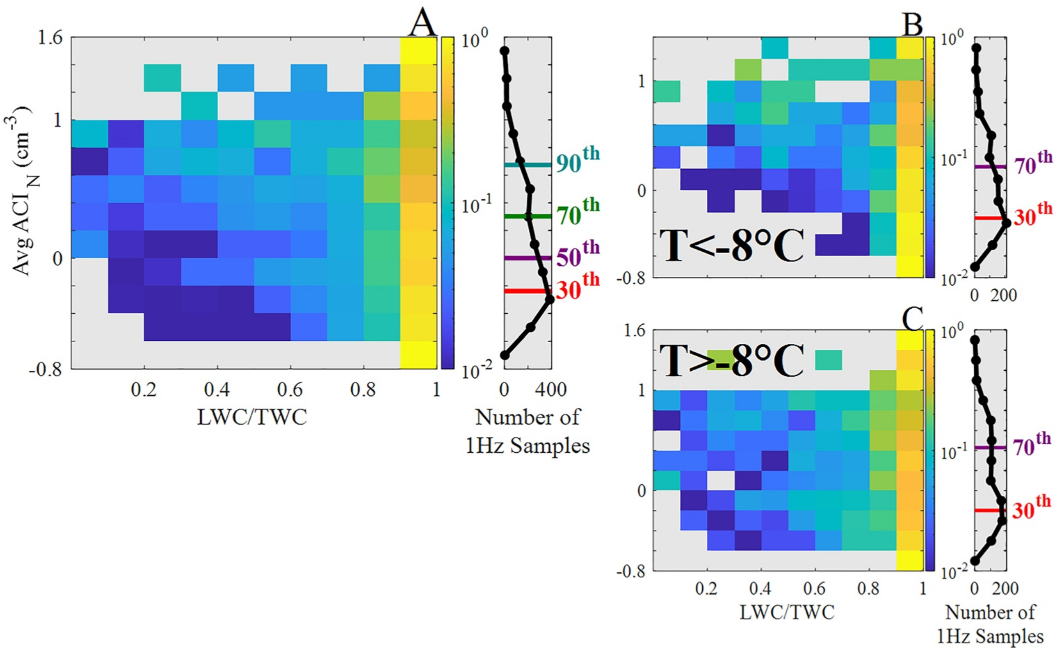

Figure 10. Normalized joint histograms relating 1 Hz mixed phase samples of liquid water content/total water content to transect average ACI_N (a) for all temperatures, (b) for temperatures less than −8°C, and (c) temperatures warmer than −8°C. Results are normalized by average ACI_N bins, where the sum of each row equals one. The number of samples for each average ACI_N bin are shown in the narrow plots immediately to the right of the respective histograms. Percentiles of average ACI_N are shown by the colored horizontal lines.

uniformly distributed at high average ACI_N. Results in Figures 10b and 10c examine the impacts of temperature related to differences such as the greater difference in liquid and ice saturation vapor pressures at lower temperatures, as well as the potential of enhanced ice particle regimes associated with secondary ice production from −3° to −8°C. Both trends mentioned above are observed for both temperature ranges, although they are much more prevalent at temperatures less than −8°C. Namely, the frequency of samples at relatively low LWC/TWC and low average ACI_N is greater at higher temperatures, which may be due to the sufficiency of weaker mixing to induce an enhanced WBF, increased riming or errors associated with misclassification of drizzle (which can appear as aspherical particles) as ice.

To explore how mixed phase PSDs vary depending on the amount of glaciation, PSDs in Figure 11 are calculated for different ranges of LWC/TWC for all average ACI_N (Figures 11a–11c) and for the upper 50th percentile of ACI_N (Figures 11d–11f). Note that sample sizes are shown in the respective panels, and the difference in sample sizes between the highest and lowest ranges of LWC/TWC decreases with increasing average ACI_N, consistent with findings in Figure 10. As previously mentioned, the liquid mass is expected to decrease whereas ice mass is expected to increase as LWC/TWC transitions from 1 to 0. This is consistent with trends in the average PSDs for all ranges of average ACI_N, where number distribution functions of particles with D greater than 200 μm are greatest for LWC/TWC < 0.4 and lowest for LWC/TWC > 0.9. Number distribution functions of particles with D < 50 μm also decrease with decreasing LWC/TWC for all average ACI_N. However, number distribution functions for D < 15 μm decrease more rapidly for the average ACI_N less than the 70th percentile compared to higher percentiles of the average ACI_N. In fact, these number distribution functions only vary by 8–30% for different LWC/TWC above the 70th percentile (Figure 11c). The difference in the number distribution function for D between 30 and 100 μm amongst difference ranges of LWC/TWC increases with increasing average ACI_N, characterized by decreasing number distribution functions for D = 100 μm. These particles are most likely droplets (based off assumptions of CDP sensitivity to spherical particles and from visual examination of 2DS imagery) which are preferentially removed at relatively high average ACI_N, suggesting larger drops are preferentially evaporating with more prominent entrainment-mixing in mixed phase clouds.

Results in Figures 11d–11f focus on differences in PSDs at relatively high ACI_N, in part to avoid the large set of drizzling samples discussed previously (Figure 7d), which appear as sharp decreases in the number distribution

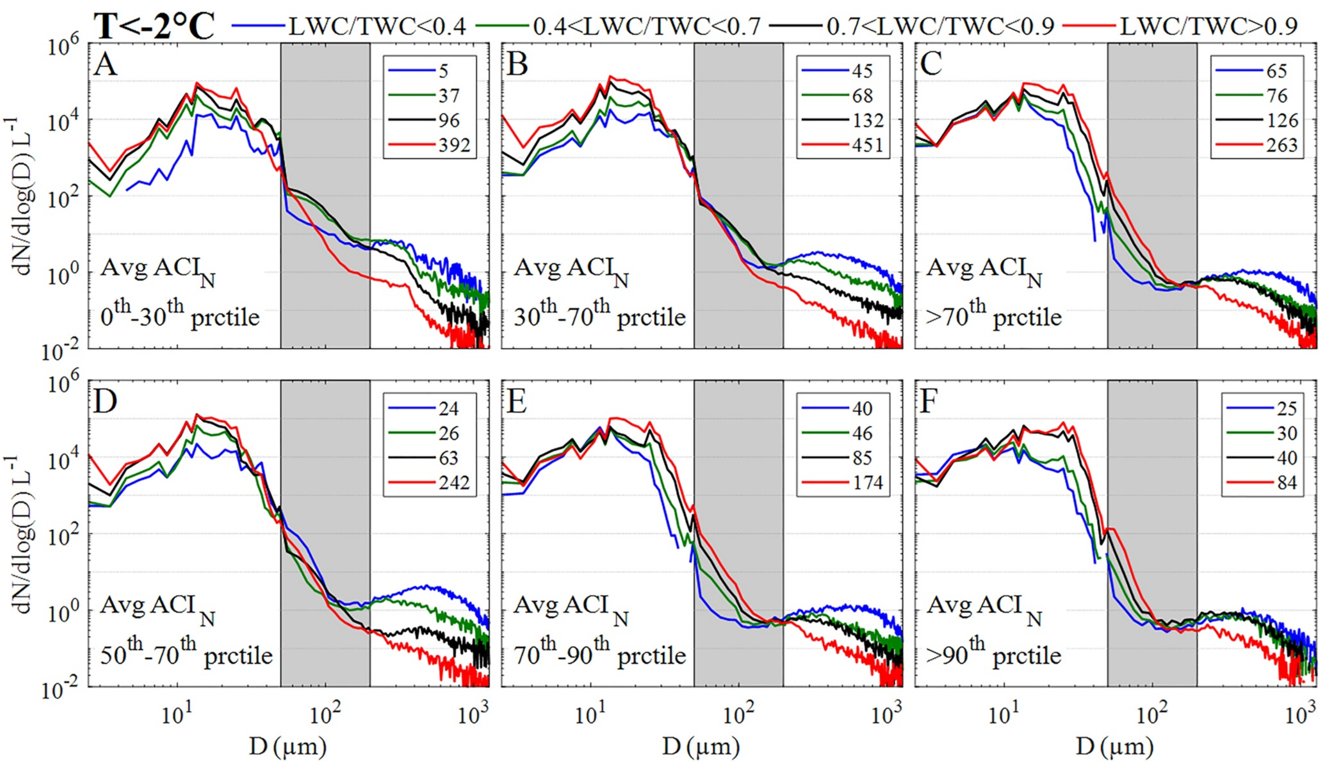

Figure 11. (a–c) Average mixed phase particle size distributions (PSDs) shown for percentiles ranging over all mixed phase samples and (d–f) for percentile ranges exceeding the 50th percentile. Colored lines represent average PSDs for different ranges of liquid water content/total water content. The number of 1 Hz mixed phase samples (contained within the respective transects) is shown in each respective panel. Results are shown for temperatures less than −2°C.

functions at D = 400 μm for average ACI_N less than the 30th percentile (Figure 11a). This is also done to account for the inability to determine when entrainment-mixing is in fact taking place (similarly discussed in reference to Figure 8). Similar trends of decreasing N(log(D)) at D < 10 μm with decreasing LWC/TWC for relatively low average ACI_N (50th to 70th percentile; Figure 11d), and decreasing number distribution functions at 100 μm with increasing average ACI_N are observed. In addition, the difference in particle sizes from 30 to 100 μm with decreasing LWC/TWC, which are primarily large drops, is much more apparent at greater average ACI_N, as the colored lines do not overlap and increasingly diverge. This is most notable at average ACI_N greater than the 90th percentile, which also has an order of magnitude difference in drop sizes from 10 to 30 μm (Figure 11f).

Although the number distribution functions of large ice (D > 200 μm) still differ for ranges of LWC/TWC above the 90th percentile of average ACI_N, they are the least variable compared to lower average ACI_N percentiles. This is consistent with evaporating drops primarily replenishing the subsaturated air resulting from substantial dry air entrainment, which may also impede ice crystal growth. In contrast, the highest number distribution functions of large ice occur at low LWC/TWC for average ACI_N between the 50th and 70th percentiles. However, there are fewer samples at low LWC/TWC for lower average ACI_N compared with higher average ACI_N. This is likely why the highest large ice concentrations occur at average ACI above the 90th percentile in Figure 8. Namely, averages at low average ACI_N are heavily weighted by samples having high LWC/TWC. These findings suggest that at substantially strong mixing, the enhanced WBF process associated with evaporating drops is partially offset by sufficiently large intrusions of dry air.

4.1. Results in Context of Cloud Morphology

Results thus far have examined entrainment-mixing regardless of cloud type and location within the clouds (e.g., cloud top, cloud base, etc.). Averaged PSDs in relation to the normalized cloud height (z_n) are shown in this section and related to the transect analysis.

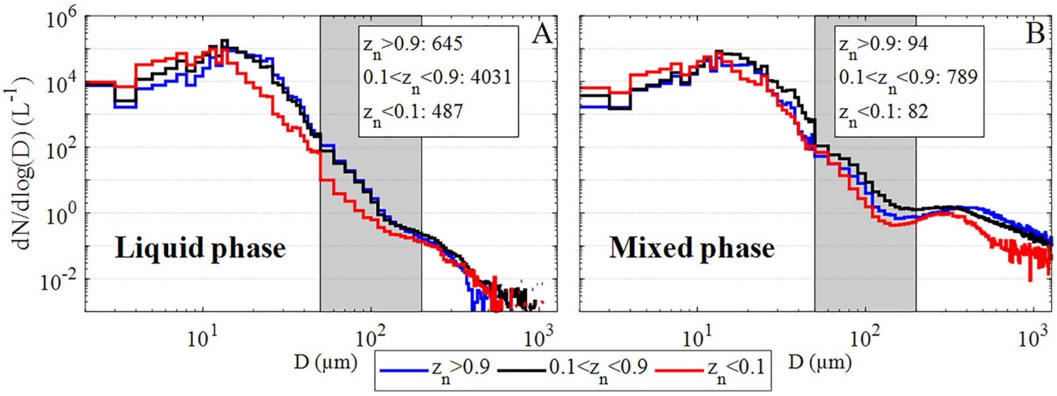

Figure 12. Average particle size distributions for (a) liquid and (b) mixed phase samples for different ranges of z_n.

Figure 12 shows average PSDs for the liquid (Figure 12a) and mixed phase (Figure 12b) samples at cloud base ($z_n < 0.1$), cloud top ($z_n > 0.9$) and within the cloud ($0.1 < z_n < 0.9$). The PSDs shift toward larger particle sizes with increasing z_n for the liquid phase, consistent with particle growth via condensation and collision-coalescence of an ascending air parcel. However, large drop number distribution functions (D > 200 μm) are nearly similar regardless of z_n. In contrast, the highest concentrations of large ice particles in mixed phase samples are observed at cloud top and are lowest near cloud base. Peak number distribution functions of large ice crystals also shift to slightly larger sizes (from 300 to 500 μm) with increasing z_n, suggesting large ice particles are preferentially growing at cloud top. It is important to note that although ACI_N are often greater at cloud top than cloud base, relatively high ACI_N occur at cloud top and cloud base (Figure 2b). Analysis of 1 Hz and average ACI_N are not controlled by normalized cloud height, so results may (perhaps likely) combine samples from both of these regions. Since large ice concentrations are found to be lowest at cloud base (Figure 12b; Figures 13b and 13c), there is the possibility for an underestimation of entrainment-mixing WBF enhancement. Regardless, these peak sizes from 300 to 500 μm are similar to those observed with relatively high average ACI_N throughout this study (e.g., Figure 8), highlighting the potential importance of entrainment-mixing on WBF process rates.

Mixed phase results are separated according to the number of cloud layers in Figure 13. PSDs from single-layer clouds are shown in Figure 13a and from multi-layer clouds in Figure 13b. The cloud layer classification follows D'Alessandro et al. (2023). Not only have mixed phase occurrence frequencies been found to be much larger in multi-layer clouds (D'Alessandro et al., 2023), but notable peaks of large ice concentrations from 300 to 500 μm are primarily observed in multi-layer clouds as well. These peaks are enhanced for middle cloud layers, defined as cloud layers residing between the highest and lowest cloud layers of multi-layer clouds (Figure 13c). D'Alessandro et al. (2023) shows air immediately overlying these middle layers is nearly saturated, whereas

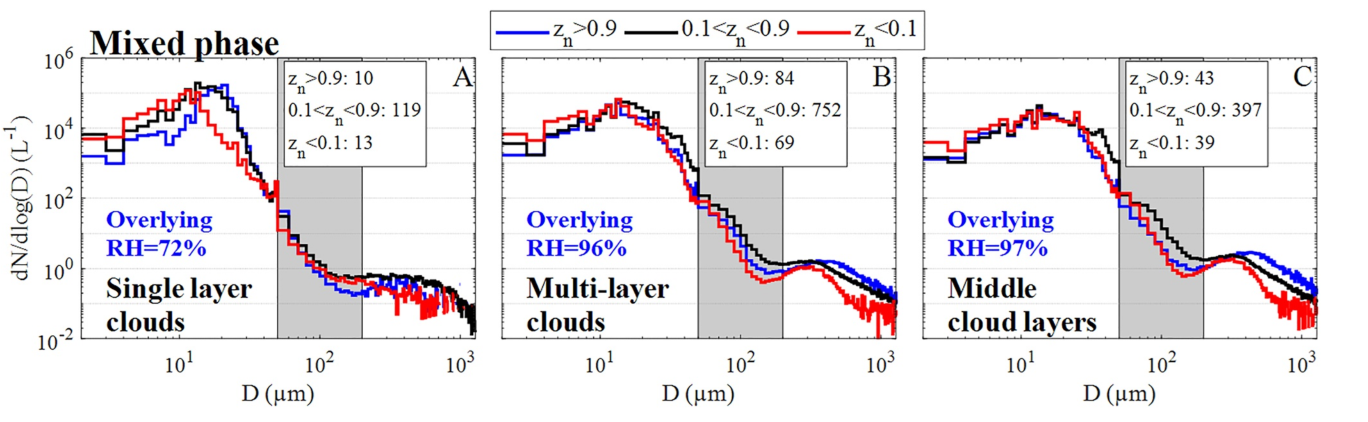

Figure 13. Similar to Figure 12, except results are only shown for mixed phase samples. Results are shown for (a) single layer clouds, (b) multi-layer clouds, and (c) middle cloud layers (residing between the highest and lowest cloud layers of multi-layer clouds). The blue text is average relative humidity immediately overlying the respective cloud layer types (taken from D'Alessandro et al. (2023)).

10.1029/2023JD038622

subsaturated conditions are commonly observed overlying single layer clouds as well as the highest layers of multi-layer clouds (blue text in Figure 13). This suggests the importance of an ample moisture supply toward ice crystal growth in entrainment-mixing events, contrary to simply considering dry air enhancing evaporation and the resulting available vapor content.

5. Overview of Findings

This study uses in situ observations from SOCRATES to provide a statistical analysis on the impacts of entrainment-mixing upon mixed phase cloud properties over the Southern Ocean. Strong correlations exist between drop clustering and the ratio of actual to adiabatic mass content at cloud tops (−0.62 to −0.74), as well as clustering and mixing length scales (0.53). These and other findings suggest clustering on scales of 100–1,000 m is primarily related to entrainment-mixing. Because of this, droplet clustering is utilized as a proxy variable for qualitatively determining the degree of mixing. Observations are split into transects, defined as regions of neighboring 1 Hz samples which range from 1.0 to 2.1 km in horizontal sampling distance. The use of transects allows for samples associated with local entrainment-mixing to be analyzed in relation to the background microphysical properties and allows for analysis on spatial scales comparable to horizontal grid spacing in weather and climate models.

Clustering is positively related to ice particle concentrations with maximum dimensions exceeding 200 μm, suggesting entrainment mixing enhances WBF process rates. Average number distribution functions associated with the highest percentiles of clustering (>70th percentiles) closely resemble those at cloud top of multi-layer clouds, suggesting entrainment-mixing is a major factor determining ice characteristics at cloud top.

Clustering is examined as a function of LWC/TWC in order to ascertain impacts of mixing on mixed phase evolution, considering that values will transition from 1 to 0 during glaciation. Distributions of LWC/TWC are heavily skewed toward 1 at minimal/non-existent clustering, and transition to more uniform distributions of LWC/TWC with increasing clustering. This trend is more pronounced at temperatures less than −8°C, where the difference in the saturation vapor pressures of liquid and ice is greater than at higher temperatures. Results suggest that a minimal amount of mixing may increase the likelihood for mixed phase samples to undergo complete glaciation on spatial scales of ∼100 m. Average PSDs are similarly examined as functions of LWC/TWC to evaluate mixed phase evolution. Drop number distribution functions between 10 and 20 μm decrease with decreasing LWC/TWC regardless of weak or prevalent clustering. At relatively low clustering, small drop number distribution functions ($D < 10$ μm) are found to decrease with decreasing LWC/TWC, which is consistent with glaciating conditions. In contrast, larger drop number distribution functions ($D > 30$ μm) are preferentially reduced with decreasing LWC/TWC when clustering is prevalent. These results suggest different drop size modes are preferentially removed during glaciation depending on the relative strength of entrainment-mixing.

6. Concluding Remarks

The goal of this study was to provide a qualitative assessment of the impact of mixing on mixed phase microphysical properties. Drop clustering has been argued to provide a simple and effective measure to broadly diagnose the strength of entrainment-mixing. In fact, previous studies have attempted to characterize entrainment-mixing and its impacts based on drop size distribution inhomogeneities (Bower & Choularton, 1988; Paluch, 1986; Paluch & Knight, 1984). Although clustering undoubtedly fails to capture the associated complexities and relevant properties of air-mass interactions, analysis here separates mixed phase properties by broad percentile ranges of clustering in order to capture the general strength of mixing and its impacts. Persistent trends (e.g., increasing number distribution functions of large ice with greater average ACI_N) combined with findings consistent with current theoretical understandings of mixing (e.g., downward shifts in average PSDs with increasing ACI_N indicative of inhomogeneous mixing, decreasing number distribution functions of large drops with increasing average ACI_N for liquid phase transects) suggest the results presented here capture the intended mixing-cloud particle interactions.

Previous studies have argued for or against different clustering metrics for reasons such as scale dependence (B. Baker & Lawson, 2010; Shaw et al., 2002). However, scale invariance is expected to be minimal since number concentrations are normalized by a constant sample volume. In addition, the clustering metric is only in service of diagnosing the magnitude of mixing. The study does not intend to provide an absolute measure of clustering but rather to inform the observational and modeling communities of potential pathways for the evolution of mixed phase microphysical properties in the presence of entrainment-mixing.

A few studies have already been introduced that discuss direct relationships of droplet clustering on local microphysical properties (Castellano et al., 2004, 2008). However, these effects are determined on much smaller spatial scales than the scale of clustering presented in this study. Regardless of these potential impacts of clustering on microphysical properties, such considerations do not nullify findings relating entrainment-mixing to mixed phase evolution. Rather, mixing likely enhances clustering which effectively impacts the microphysical properties. For example, clustering resulting from dry air insertion may lead to enhanced evaporation of droplets near the edges of drop clusters due to differences in the local vapor density fields within clusters and near cluster edges (Castellano & Ávila, 2011). It may prove helpful to disseminate direct impacts of mixing and clustering on mixed phase properties.

Clustering is calculated on spatial scales orders of magnitude greater (100 m) than those considered in most of the theoretical clustering studies listed here (∼1 cm). Commonly deployed in situ instrumentation for most field campaigns, including SOCRATES, are unable to determine clustering at finer spatial scales. Such probes require averaging over relatively long durations to compensate for the instruments' inherent lack of ergodicity. Other probes, such as the Holographic Detector for Clouds (HOLODEC), have the advantage of obtaining size distributions by imaging a constant volume sample field. Few intercomparisons between these instruments have been performed (e.g., Beals et al., 2015; Glienke et al., 2017; Jackson et al., 2014), and those comparing varying scales of clustering are warranted in order to disseminate primary and secondary causes impacting mixed phase properties. The HOLODEC would also be advantageous for characterizing particle phase from 50 to 100 μm, due to the inability of the 2DS to adequately diagnose sphericity with the relatively coarse resolution of the diode array.

Future work should aim to constrain mixing properties by directly relating entrainment rates with mixed phase properties at cloud top. Similar work evaluating entrainment-mixing is warranted for different cloud types and regions globally, which will be associated with varying atmospheric phenomenon, turbulent features, and mixed phase properties. Additional work should also explore the impacts of phase inhomogeneity on the potential enhancement of WBF within the length scale of mixed phase observations (∼100 m) used here.

Appendix A: Equations Used to Determine Da

The turbulent dissipation is taken from Paluch and Baumgardner (1989) and shown as:

$$\varepsilon = \frac{\mathrm{D_{NN}}^{\frac{3}{2}}}{(4.01b)^{\frac{3}{2}}\, l_e} \tag{A1}$$

where $b \approx 0.2(2\pi)^{2/3}$ (taken from Panofsky and Dutton (1984)), l_e is the length scale and $\mathrm{D_{NN}}$ is taken from Meischner et al. (2001) and shown as:

$$\mathrm{D_{NN}}(t,\mathrm{TAS}) = \frac{1}{3}\left\{\begin{array}{c}\frac{8}{7}\left[u(t) - u\left(t - \frac{l_e}{\mathrm{TAS}}\right)\right]^2 + \frac{8}{7}\left[v(t) - v\left(t - \frac{l_e}{\mathrm{TAS}}\right)\right]^2 + \\ \left[w(t) - w\left(t - \frac{l_e}{\mathrm{TAS}}\right)\right]^2\end{array}\right\} \tag{A2}$$

and additional terms are defined in Appendix B. The phase relaxation times used to determine Da are taken from Pinsky et al. (2018), although the phase relaxation time for the liquid phase has been introduced in earlier studies (Korolev & Mazin, 2003; Pinsky et al., 2015) and is expressed as:

$$\tau_{\mathrm{phase},w} = \left(\frac{4\pi\rho_w \mathrm{A}_2}{\rho_a \mathrm{F}_w}\mathrm{N}_w \overline{r_w}\right)^{-1} \tag{A3}$$

where A_2 is expressed as:

$$\mathrm{A}_2 = \frac{1}{q_v} + \frac{\mathrm{L}_w{}^2}{c_p \mathrm{R_v} \mathrm{T}^2} \tag{A4}$$

and F_w is expressed as:

$$F_w = \frac{\rho_w {L_w}^2}{KR_vT^2} + \frac{\rho_w R_v T}{e_w D_e} \tag{A5}$$

and additional terms are defined in Appendix B. To derive the phase relaxation time for the mixed phase, the phase relaxation time for the ice is used (Korolev & Mazin, 2003; Pinsky et al., 2015) and expressed as:

$$\tau_{\text{phase},i} = \left(\frac{4\pi\rho_i A_3 \varphi}{\rho_i F_i} N_i \overline{r_i}\right)^{-1} \tag{A6}$$

where A_3 is expressed as:

$$A_3 = \frac{1}{q_v} + \frac{L_w L_i}{c_p R_v T^2} \tag{A7}$$

and F_i is expressed as:

$$F_i = \frac{\rho_i {L_i}^2}{KR_vT^2} + \frac{\rho_i R_v T}{e_i D_e} \tag{A8}$$

and additional terms are defined in Appendix B. The phase relaxation times of the liquid and ice phase are combined to determine the relaxation time for the mixed phase (Pinsky et al., 2018) and is expressed as:

$$\tau_{\text{phase},m} = \frac{\tau_{\text{phase},w}\tau_{\text{phase},i}}{\left(\tau_{\text{phase},w} + \tau_{\text{phase},i}\right)} \tag{A9}$$

The shorter microphysical response time between the phase relaxation and evaporation times is selected when determine L*. The evaporation time for the liquid is taken from Rogers and Yau (1996) and is expressed as:

$$\tau_{\text{evap}} = -\frac{{r_m}^2}{2As} \tag{A10}$$

where A is expressed as:

$$A = \frac{1}{\left[\left(\frac{L_w}{R_vT} - 1\right)\frac{L_w\rho_w}{KT} + \frac{\rho_w R_v T}{D_e e_w}\right]} \tag{A11}$$

The evaporation time for the mixed phase is defined as the time for complete glaciation to occur within a mixed phase cloud (Hoffmann, 2020), which is expressed as:

$$\tau_{\text{gl}} = \frac{3}{2}\tau_{\text{phase},i}\frac{q_l}{(q_{s,l} - q_{s,i})} \tag{A12}$$

and additional terms are defined in Appendix B.

Appendix B: Table of Contents

Symbol	Description
ACI	Altered Clustering Index
AVAPC	Altered Volume Average Pair Correlation
CI	Clustering Index
D	Maximum particle dimension

Symbol	Description
Da	Damköhler number
D_e	Coefficient of diffusion of water vapor in air
e_i	Saturation vapor pressure for ice
e_w	Saturation vapor pressure for liquid water
F	Clear sky fraction
f	Sampling frequency
K	Coefficient of thermal conductivity of air
L	Mixing length scale
L_i	Latent heat of sublimation
L_w	Latent heat of vaporization
L*	Transition length scale
LWC	Liquid water content
l_e	Length scale
M	Mass content
Mean D	Number weighted mean diameter
N	Number concentration
N_i	Ice number concentration
N_w	Liquid number concentrations
q_l	Liquid water mixing ratio
$q_{s,i}$	Ice saturation vapor mixing ratio
$q_{s,l}$	Liquid water saturation vapor mixing ratio
q_v	Water vapor mixing ratio
R_v	Gas constant for water vapor
r_i	Ice particle radius
r_w	Liquid particle radius
r_m	Number weighted mean radius
r_v	Volume weighted mean radius
s	Supersaturation
t	Time
u	East wind component
v	North wind component
TAS	True air speed
TWC	Total condensed water content
VAPC	Volume Average Pair Correlation
w	Vertical air motion
z	Altitude
z_{cloud_top}	Cloud top altitude
z_{cloud_base}	Cloud base altitude
z_n	Normalized height
ε	turbulent dissipation rate
τ_{evap}	Evaporation time
τ_{gl}	Time for glaciation of mixed phase cloud
τ_m	Turbulent mixing time
τ_{phase}	Phase relaxation time

Symbol	Description
$\tau_{\text{phase},i}$	Ice phase relaxation time
$\tau_{\text{phase},m}$	Mixed phase relaxation time
$\tau_{\text{phase},w}$	Liquid phase relaxation time
τ_r	Microphysics response time
τ_{react}	Reaction time
ρ_a	Density of air
ρ_i	Density of ice
ρ_w	Density of liquid water
φ	e_w/e_i

Data Availability Statement

The data were collected using NSF's Lower Atmosphere Observing Facilities, which are managed and operated by NCAR's Earth Observing Laboratory. The NSF SOCRATES campaign dataset is publicly available and can be accessed at http://www.eol.ucar.edu/field_projects/socrates. Data includes 2DS PSDs (Wu & McFarquhar, 2019), raw 2DS particle imagery (NCAR/EOL, 2018) and alternative in situ instrumentation (NCAR/EOL, 2022).

Acknowledgments

This work was supported by the National Science Foundation (NSF) through Grants AGS-1628674 and AGS-1762096. This material is based upon work supported by the National Center for Atmospheric Research, which is a major facility sponsored by the NSF under Cooperative Agreement No. 1852977. We thank the pilots, mechanics, technicians, scientists, software engineers, and project managers of the NCAR EOL Research Aviation Facility for their support in the field and in post-processing data. We would like to thank the Australian Bureau of Meteorology Tasmanian regional Office for the excellent forecast support and weather briefings provided during the field campaign with special thanks to Scott Carpentier, Michelle Hollister, Matthew Thomas, and Robert Schaap. We also thank Dr. Jeffrey L. Stith for providing valuable input and insight, which significantly improved the study overall.

References

Andrejczuk, M., Grabowski, W. W., Malinowski, S. P., & Smolarkiewicz, P. K. (2009). Numerical simulation of cloud-clear air interfacial mixing: Homogeneous versus inhomogeneous mixing. *Journal of the Atmospheric Sciences*, *66*(8), 2493–2500. https://doi.org/10.1175/2009JAS2956.1

Baker, B. A., & Lawson, R. P. (2010). Analysis of tools used to quantify droplet clustering in clouds. *Journal of the Atmospheric Sciences*, *67*(10), 3355–3367. https://doi.org/10.1175/2010JAS3409.1

Baker, B. A. (1992). Turbulent entrainment and mixing in clouds: A new observational approach. *Journal of the Atmospheric Sciences*, *49*(5), 387–404. https://doi.org/10.1175/1520-0469(1992)049<0387:TEAMIC>2.0.CO;2

Baker, M. B., Corbin, R. G., & Latham, J. (1980). The influence of entrainment on the evolution of cloud droplet spectra: I. A model of inhomogeneous mixing. *Quarterly Journal of the Royal Meteorological Society*, *106*(449), 581–598. https://doi.org/10.1002/qj.49710644914

Baumgardner, D., Abel, S. J., Axisa, D., Cotton, R., Crosier, J., Field, P., et al. (2017). Cloud ice properties: In situ measurement challenges. *Meteorological Monographs*, *58*(1), 9.1–9.23. https://doi.org/10.1175/amsmonographs-d-16-0011.1

Baumgardner, D., & Korolev, A. (1997). Airspeed corrections for optical array probe sample volumes. *Journal of Atmospheric and Oceanic Technology*, *14*(5), 1224–1229. https://doi.org/10.1175/1520-0426(1997)014<1224:ACFOAP>2.0.CO;2

Beals, M. J., Fugal, J. P., Shaw, R. A., Lu, J., Spuler, S. M., & Stith, J. L. (2015). Holographic measurements of inhomogeneous cloud mixing at the centimeter scale. *Science*, *350*(6256), 87–90. https://doi.org/10.1126/science.aab0751

Bergeron, T. (1928). Über die dreidimensional verknüpfende Wetteranalyse. *Geophysica Norvegica*, *5*(6), 1–111.

Bodas-Salcedo, A., Hill, P. G., Furtado, K., Williams, K. D., Field, P. R., Manners, J. C., et al. (2016). Large contribution of supercooled liquid clouds to the solar radiation budget of the Southern Ocean. *Journal of Climate*, *29*(11), 4213–4228. https://doi.org/10.1175/JCLI-D-15-0564.1

Bower, K. N., & Choularton, T. W. (1988). The effects of entrainment on the growth of droplets in continental cumulus clouds. *Quarterly Journal of the Royal Meteorological Society*, *114*(484), 1411–1434. https://doi.org/10.1002/qj.49711448404

Braun, R. A., Dadashazar, H., MacDonald, A. B., Crosbie, E., Jonsson, H. H., Woods, R. K., et al. (2018). Cloud adiabaticity and its relationship to marine stratocumulus characteristics over the northeast Pacific Ocean. *Journal of Geophysical Research: Atmospheres*, *123*(24), 13790–13806. https://doi.org/10.1029/2018JD029287

Burnet, F., & Brenguier, J. L. (2007). Observational study of the entrainment-mixing process in warm convective clouds. *Journal of the Atmospheric Sciences*, *64*(6), 1995–2011. https://doi.org/10.1175/JAS3928.1

Castellano, N. E., & Ávila, E. E. (2011). Vapour density field of a population of cloud droplets. *Journal of Atmospheric and Solar-Terrestrial Physics*, *73*(16), 2423–2428. https://doi.org/10.1016/j.jastp.2011.08.013

Castellano, N. E., Avila, E. E., & Saunders, C. P. R. (2004). Theoretical model of the Bergeron-Findeisen mechanism of ice crystal growth in clouds. *Atmospheric Environment*, *38*(39), 6751–6761. https://doi.org/10.1016/j.atmosenv.2004.09.003

Castellano, N. E., Ávila, E. E., & Saunders, C. P. R. (2008). Vapour density field of mixed-phase clouds. *Atmospheric Research*, *88*(1), 56–65. https://doi.org/10.1016/j.atmosres.2007.10.002

Chen, Y. C., Xue, L., Lebo, Z. J., Wang, H., Rasmussen, R. M., & Seinfeld, J. H. (2011). A comprehensive numerical study of aerosol-cloud-precipitation interactions in marine stratocumulus. *Atmospheric Chemistry and Physics*, *11*(18), 9749–9769. https://doi.org/10.5194/acp-11-9749-2011

Cober, S. G., & Isaac, G. A. (2012). Characterization of aircraft icing environments with supercooled large drops for application to commercial aircraft certification. *Journal of Applied Meteorology and Climatology*, *51*(2), 265–284. https://doi.org/10.1175/JAMC-D-11-022.1

Cooper, W. A., Friesen, R. B., Hayman, M., Jensen, J. B., Lenschow, D. H., Romashkin, P. A., et al. (2016). Characterization of uncertainty in measurements of wind from the NSF/NCAR Gulfstream V research aircraft. Retrieved from https://opensky.ucar.edu/islandora/object/technotes%3A540/datastream/PDF/download/Characterization_of_Uncertainty_in_Measurements_of_Wind_from_the_NSF_NCAR_Gulfstream_V_Research_Aircraft.citation

Cossich, W., Maestri, T., Magurno, D., Martinazzo, M., Di Natale, G., Palchetti, L., et al. (2021). Ice and mixed-phase cloud statistics on the Antarctic Plateau. *Atmospheric Chemistry and Physics*, *21*(18), 13811–13833. https://doi.org/10.5194/acp-21-13811-2021

Costa, A., Meyer, J., Afchine, A., Luebke, A., Günther, G., Dorsey, J. R., et al. (2017). Classification of Arctic, midlatitude and tropical clouds in the mixed-phase temperature regime. *Atmospheric Chemistry and Physics*, *17*(19), 12219–12238. https://doi.org/10.5194/acp-17-12219-2017

D'Alessandro, J. J., Diao, M., Wu, C., Liu, X., Jensen, J. B., & Stephens, B. B. (2019). Cloud phase and relative humidity distributions over the Southern Ocean in austral summer based on in situ observations and CAM5 simulations. *Journal of Climate*, *32*(10), 2781–2805. https://doi.org/10.1175/JCLI-D-18-0232.1

D'Alessandro, J. J., Mcfarquhar, G. M., Stith, J. L., Jensen, J. B., Diao, M., DeMott, P. J., & Sanchez, K. J. (2023). An evaluation of phase, aerosol-cloud interactions and microphysical properties of single- and multi-layer clouds over the Southern Ocean using in situ observations from SOCRATES. *Journal of Geophysical Research: Atmospheres*. https://doi.org/10.1029/2023JD038610

D'Alessandro, J. J., McFarquhar, G. M., Wu, W., Stith, J. L., Jensen, J. B., & Rauber, R. M. (2021). Characterizing the occurrence and spatial heterogeneity of liquid, ice, and mixed phase low-level clouds over the Southern Ocean using in situ observations acquired during SOCRATES. *Journal of Geophysical Research: Atmospheres*, *126*(11), e2020JD034482. https://doi.org/10.1029/2020JD034482

Damköhler, G. Z. (1940). Influence of turbulence on flame velocity in gaseous mixtures. *ZH Electrochem*, *46*, 601–626.

Devenish, B. J., Bartello, P., Brenguier, J.-L., Collins, L. R., Grabowski, W. W., Ijzermans, R. H. A., et al. (2012). Droplet growth in warm turbulent clouds. *Quarterly Journal of the Royal Meteorological Society*, *138*(667), 1401–1429. https://doi.org/10.1002/qj.1897

Diao, M. (2021). VCSEL 1 Hz water vapor data: UCAR/NCAR—Earth Observing Laboratory. Retrieved from https://data.eol.ucar.edu/dataset/552.051

Dimotakis, P. E. (2005). Turbulent mixing. *Annual Review of Fluid Mechanics*, *37*(1), 329–356. https://doi.org/10.1146/annurev.fluid.36.050802.122015

Dodson, D. S., & Small Griswold, J. D. (2019). Droplet inhomogeneity in shallow cumuli: The effects of in-cloud location and aerosol number concentration. *Atmospheric Chemistry and Physics*, *19*(11), 7297–7317. https://doi.org/10.5194/acp-19-7297-2019

Earth Observing Laboratory. (2018). Retrieved from https://www.eol.ucar.edu/system/files/SOCRATES%20PM%20Report.pdf

Field, P. R., Heymsfield, A. J., & Bansemer, A. (2006). Shattering and particle interarrival times measured by optical array probes in ice clouds. *Journal of Atmospheric and Oceanic Technology*, *23*(10), 1357–1371. https://doi.org/10.1175/JTECH1922.1

Field, P. R., Wood, R., Brown, P. R. A., Kaye, P. H., Hirst, E., Greenaway, R., & Smith, J. A. (2003). Ice particle interarrival times measured with a fast FSSP. *Journal of Atmospheric and Oceanic Technology*, *20*(2), 249–261. https://doi.org/10.1175/1520-0426(2003)020<0249:IPITMW>2.0.CO;2

Findeisen, W. (1938). Kolloid-meteorologische Vorgänge bei Neiderschlags-bildung. *Meteorologische Zeitschrift*, *55*, 121–133.

Finlon, J. A., McFarquhar, G. M., Nesbitt, S. W., Rauber, R. M., Morrison, H., Wu, W., & Zhang, P. (2019). A novel approach for characterizing the variability in mass–dimension relationships: Results from MC3E. *Atmospheric Chemistry and Physics*, *19*(6), 3621–3643. https://doi.org/10.5194/acp-19-3621-2019

Gao, S., Lu, C., Liu, Y., Yum, S. S., Zhu, J., Zhu, L., et al. (2021). Comprehensive quantification of height dependence of entrainment mixing between stratiform cloud top and environment. *Atmospheric Chemistry and Physics*, *21*(14), 11225–11241. https://doi.org/10.5194/acp-21-11225-2021

Gao, Z., Liu, Y., Li, X., & Lu, C. (2018). Investigation of turbulent entrainment-mixing processes with a new particle-resolved direct numerical simulation model. *Journal of Geophysical Research: Atmospheres*, *123*(4), 2194–2214. https://doi.org/10.1002/2017JD027507

Gerber, H. E., Frick, G. M., Jensen, J. B., & Hudson, J. G. (2008). Entrainment, mixing, and microphysics in trade-wind cumulus. *Journal of the Meteorological Society of Japan*, *86A*, 87–106. https://doi.org/10.2151/jmsj.86a.87

Gettelman, A., Bardeen, C. G., McCluskey, C. S., Järvinen, E., Stith, J., Bretherton, C., et al. (2020). Simulating observations of Southern Ocean clouds and implications for climate. *Journal of Geophysical Research: Atmospheres*, *125*(21), e2020JD032619. https://doi.org/10.1029/2020JD032619

Glienke, S., Kostinski, A., Fugal, J., Shaw, R. A., Borrmann, S., & Stith, J. (2017). Cloud droplets to drizzle: Contribution of transition drops to microphysical and optical properties of marine stratocumulus clouds. *Geophysical Research Letters*, *44*(15), 8002–8010. https://doi.org/10.1002/2017GL074430

Grabowski, W. W., & Wang, L.-P. (2013). Growth of cloud droplets in a turbulent environment. *Annual Review of Fluid Mechanics*, *45*(1), 293–324. https://doi.org/10.1146/annurev-fluid-011212-140750

Hallett, J., & Mossop, S. C. (1974). Production of secondary ice particles during the riming process. *Nature*, *249*(5452), 26–28. https://doi.org/10.1038/249026a0

Heymsfield, A. J. (1977). Precipitation development in stratiform ice clouds: A microphysical and dynamical study. *Journal of the Atmospheric Sciences*, *34*(2), 367–381. https://doi.org/10.1175/1520-0469(1977)034<0367:PDISIC>2.0.CO;2

Heymsfield, A. J., Field, P. R., Bailey, M., Rogers, D., Stith, J., Twohy, C., et al. (2011). Ice in clouds experiment-layer clouds. Part I: Ice growth rates derived from lenticular wave cloud penetrations. *Journal of the Atmospheric Sciences*, *68*(11), 2628–2654. https://doi.org/10.1175/JAS-D-11-025.1

Heymsfield, A. J., & Parrish, J. L. (1978). Computation technique for increasing the effective sampling volume of the PMS two-dimensional particle size spectrometer. *Journal of Applied Meteorology*, *17*(10), 1566–1572. https://doi.org/10.1175/1520-0450(1978)017<1566:ACTFIT>2.0.CO;2

Hill, A. A., Field, P. R., Furtado, K., Korolev, A., & Shipway, B. J. (2014). Mixed-phase clouds in a turbulent environment. Part 1: Large-eddy simulation experiments. *Quarterly Journal of the Royal Meteorological Society*, *140*(680), 855–869. https://doi.org/10.1002/qj.2177

Hoffmann, F. (2020). Effects of entrainment and mixing on the Wegener-Bergeron-Findeisen process. *Journal of the Atmospheric Sciences*, *77*(6), 2279–2296. https://doi.org/10.1175/JAS-D-19-0289.1

Hogan, R. J., Illingworth, A. J., O'Connor, E. J., & PoiaresBaptista, J. P. V. (2003). Characteristics of mixed-phase clouds. II: A climatology from ground-based lidar. *Quarterly Journal of the Royal Meteorological Society*, *129*(592), 2117–2134. https://doi.org/10.1256/qj.01.209

Holroyd, E. W. (1987). Some techniques and uses of 2D-C habit classification software for snow particles. *Journal of Atmospheric and Oceanic Technology*, *4*(3), 498–511. https://doi.org/10.1175/1520-0426(1987)004<0498:stauoc>2.0.co;2

Houze, R. A. (2014). Cloud dynamics - Second edition. In *International Geophysics* (Vol. 104, pp. 1–432). Academic Press. https://doi.org/10.1016/B978-0-12-374266-7.00001-9

Huang, Y., Siems, S. T., & Manton, M. J. (2021). Wintertime in situ cloud microphysical properties of mixed-phase clouds over the Southern Ocean. *Journal of Geophysical Research: Atmospheres*, *126*(11), e2021JD034832. https://doi.org/10.1029/2021JD034832

Huang, Y., Siems, S. T., Manton, M. J., Hande, L. B., & Haynes, J. M. (2012). The structure of low-altitude clouds over the Southern Ocean as seen by CloudSat. *Journal of Climate*, *25*(7), 2535–2546. https://doi.org/10.1175/JCLI-D-11-00131.1

Jackson, R. C., McFarquhar, G. M., Korolev, A. V., Earle, M. E., Liu, P. S. K., Lawson, R. P., et al. (2012). The dependence of ice microphysics on aerosol concentration in arctic mixed-phase stratus clouds during ISDAC and M-PACE. *Journal of Geophysical Research*, *117*(15), D15207. https://doi.org/10.1029/2012JD017668

Jackson, R. C., Mcfarquhar, G. M., Stith, J., Beals, M., Shaw, R. A., Jensen, J., et al. (2014). An assessment of the impact of antishattering tips and artifact removal techniques on cloud ice size distributions measured by the 2D cloud probe. *Journal of Atmospheric and Oceanic Technology*, *31*(12), 2567–2590. https://doi.org/10.1175/JTECH-D-13-00239.1

Jensen, J. B., & Baker, M. B. (1989). A simple model of droplet spectral evolution during turbulent mixing. *Journal of the Atmospheric Sciences*, *46*(18), 2812–2829. https://doi.org/10.1175/1520-0469(1989)046<2812:ASMODS>2.0.CO;2

Jia, H., Ma, X., & Liu, Y. (2019). Exploring aerosol-cloud interaction using VOCALS-REx aircraft measurements. *Atmospheric Chemistry and Physics*, *19*(12), 7955–7971. https://doi.org/10.5194/acp-19-7955-2019

Korolev, A. V., Khain, A., Pinsky, M., & French, J. (2016). Theoretical study of mixing in liquid clouds-Part 1: Classical concepts. *Atmospheric Chemistry and Physics*, *16*(14), 9235–9254. https://doi.org/10.5194/acp-16-9235-2016

Korolev, A. V., McFarquhar, G., Field, P. R., Franklin, C., Lawson, P., Wang, Z., et al. (2017). Mixed-phase clouds: Progress and challenges. *Meteorological Monographs*, *58*, 5.1–5.50. https://doi.org/10.1175/AMSMONOGRAPHS-D-17-0001.1

Korolev, A. V., Isaac, G. A., Cober, S. G., Strapp, J. W., & Hallett, J. (2003). Microphysical characterization of mixed-phase clouds. *Quarterly Journal of the Royal Meteorological Society*, *129*(587), 39–65. https://doi.org/10.1256/qj.01.204

Korolev, A. V., & Mazin, I. P. (2003). Supersaturation of water vapor in clouds. *Journal of the Atmospheric Sciences*, *60*(24), 2957–2974. https://doi.org/10.1175/1520-0469(2003)060<2957:SOWVIC>2.0.CO;2

Kumar, B., Götzfried, P., Suresh, N., Schumacher, J., & Shaw, R. A. (2018). Scale dependence of cloud microphysical response to turbulent entrainment and mixing. *Journal of Advances in Modeling Earth Systems*, *10*(11), 2777–2785. https://doi.org/10.1029/2018MS001487

Kumar, B., Schumacher, J., & Shaw, R. A. (2014). Lagrangian mixing dynamics at the cloudy-clear air interface. *Journal of the Atmospheric Sciences*, *71*(7), 2564–2580. https://doi.org/10.1175/JAS-D-13-0294.1

Lance, S., Brock, C. A., Rogers, D., & Gordon, J. A. (2010). Water droplet calibration of the Cloud Droplet Probe (CDP) and in-flight performance in liquid, ice and mixed-phase clouds during ARCPAC. *Atmospheric Measurement Techniques*, *3*(6), 1683–1706. https://doi.org/10.5194/amt-3-1683-2010

Lasher-Trapp, S. G., Cooper, W. A., & Blyth, A. M. (2005). Broadening of droplet size distributions from entrainment and mixing in a cumulus cloud. *Quarterly Journal of the Royal Meteorological Society*, *131*(605), 195–220. https://doi.org/10.1256/qj.03.199

Latham, J., & Reed, R. L. (1977). Laboratory studies of the effects of mixing on the evolution of cloud droplet spectra. *Quarterly Journal of the Royal Meteorological Society*, *103*(436), 297–306. https://doi.org/10.1002/qj.49710343607

Lehmann, K., Siebert, H., & Shaw, R. A. (2009). Homogeneous and inhomogeneous mixing in cumulus clouds: Dependence on local turbulence structure. *Journal of the Atmospheric Sciences*, *66*(12), 3641–3659. https://doi.org/10.1175/2009JAS3012.1

Lu, C., Liu, Y., & Niu, S. (2011). Examination of turbulent entrainment-mixing mechanisms using a combined approach. *Journal of Geophysical Research*, *116*(D20), D20207. https://doi.org/10.1029/2011JD015944

Lu, C., Liu, Y., Zhu, B., Yum, S. S., Krueger, S. K., Qiu, Y., et al. (2018). On which microphysical time scales to use in studies of entrainment-mixing mechanisms in clouds. *Journal of Geophysical Research: Atmospheres*, *123*(7), 3740–3756. https://doi.org/10.1002/2017JD027985

Mace, G. G., Protat, A., & Benson, S. (2021). Mixed-phase clouds over the Southern Ocean as observed from satellite and surface based lidar and radar. *Journal of Geophysical Research: Atmospheres*, *126*(16), e2021JD034569. https://doi.org/10.1029/2021JD034569

McFarquhar, G. M. (2004). The effect of raindrop clustering on collision-induced break-up of raindrops. *Quarterly Journal of the Royal Meteorological Society*, *130*(601), 2169–2190. https://doi.org/10.1256/qj.03.98

McFarquhar, G. M., Baumgardner, D., Bansemer, A., Abel, S. J., Crosier, J., French, J., et al. (2017). Processing of ice cloud in situ data collected by bulk water, scattering, and imaging probes: Fundamentals, uncertainties, and efforts toward consistency. *Meteorological Monographs*, *58*, 11.1–11.33. https://doi.org/10.1175/amsmonographs-d-16-0007.1

McFarquhar, G. M., Bretherton, C., Marchand, R., Protat, A., DeMott, P. J., Alexander, S. P., et al. (2021). Observations of clouds, aerosols, precipitation, and surface radiation over the Southern Ocean: An overview of CAPRICORN, MARCUS, MICRE and SOCRATES. *Bulletin of the American Meteorological Society*, *102*(4), E894–E928. https://doi.org/10.1175/bams-d-20-0132.1

McFarquhar, G. M., Finlon, J. A., Stechman, D. M., Wu, W., Jackson, R., & Freer, M. (2018). University of Illinois/Oklahoma Optical Array Probe (OAP) processing software. Version 3.1.4 [Dataset]. Zenodo. https://doi.org/10.5281/zenodo.1285968

McFarquhar, G. M., Zhang, G., Poellot, M. R., Kok, G. L., McCoy, R., Tooman, T., et al. (2007). Ice properties of single-layer stratocumulus during the Mixed-Phase Arctic Cloud Experiment: 1. Observations. *Journal of Geophysical Research*, *112*(D24), D24201. https://doi.org/10.1029/2007JD008633

Meischner, P., Baumann, R., Höller, H., & Jank, T. (2001). Eddy dissipation rates in thunderstorms estimated by Doppler radar in relation to aircraft in situ measurements. *Journal of Atmospheric and Oceanic Technology*, *18*(10), 1609–1627. https://doi.org/10.1175/1520-0426(2001)018<1609:EDRITE>2.0.CO;2

Mellado, J. P. (2017). Cloud-top entrainment in stratocumulus clouds. *Annual Review of Fluid Mechanics*, *49*(1), 145–169. https://doi.org/10.1146/annurev-fluid-010816-060231

Mioche, G., Jourdan, O., Ceccaldi, M., & Delanoë, J. (2015). Variability of mixed-phase clouds in the Arctic with a focus on the Svalbard region: A study based on spaceborne active remote sensing. *Atmospheric Chemistry and Physics*, *15*(5), 2445–2461. https://doi.org/10.5194/acp-15-2445-2015

Morrison, A. E., Siems, S. T., & Manton, M. J. (2011). A three-year climatology of cloud-top phase over the Southern Ocean and North Pacific. *Journal of Climate*, *24*(9), 2405–2418. https://doi.org/10.1175/2010JCLI3842.1

Morrison, H., de Boer, G., Feingold, G., Harrington, J., Shupe, M. D., & Sulia, K. (2012). Resilience of persistent Arctic mixed-phase clouds. *Nature Geoscience*, *5*(1), 11–17. https://doi.org/10.1038/ngeo1332

Mülmenstädt, J., Sourdeval, O., Delanoë, J., & Quaas, J. (2015). Frequency of occurrence of rain from liquid-mixed-and ice-phase clouds derived from A-Train satellite retrievals. *Geophysical Research Letters*, *42*(15), 6502–6509. https://doi.org/10.1002/2015GL064604

Murphy, D. M., & Koop, T. (2005). Review of the vapour pressures of ice and supercooled water for atmospheric applications. *Quarterly Journal of the Royal Meteorological Society*, *131*(608), 1539–1565. https://doi.org/10.1256/qj.04.94

Naud, C. M., Booth, J. F., & Del Genio, A. D. (2014). Evaluation of ERA-Interim and MERRA cloudiness in the southern ocean. *Journal of Climate*, *27*(5), 2109–2124. https://doi.org/10.1175/JCLI-D-13-00432.1

Paluch, I. R. (1986). Mixing and the cloud droplet size spectrum: Generalizations from the CCOPE data. *Journal of the Atmospheric Sciences*, *43*(18), 1984–1993. https://doi.org/10.1175/1520-0469(1986)043<1984:MATCDS>2.0.CO;2

Paluch, I. R., & Baumgardner, D. G. (1989). Entrainment and fine-scale mixing in a continental convective cloud. *Journal of the Atmospheric Sciences*, *46*(2), 261–278. https://doi.org/10.1175/1520-0469(1989)046<0261:EAFSMI>2.0.CO;2

Paluch, I. R., & Knight, C. A. (1984). Mixing and the evolution of cloud droplet size spectra in a vigorous continental cumulus. *Journal of the Atmospheric Sciences*, *41*(11), 1801–1815. https://doi.org/10.1175/1520-0469(1984)041<1801:MATEOC>2.0.CO;2

Panofsky, H. A., & Dutton, J. A. (1984). Atmospheric turbulence models and methods for engineering applications. Retrieved from http://www.sciepub.com/reference/40493

Pawlowska, H., Brenguier, J. L., & Burnet, F. (2000). Microphysical properties of stratocumulus clouds. *Atmospheric Research*, *55*(1), 15–33. https://doi.org/10.1016/S0169-8095(00)00054-5

Pinsky, M., Khain, A., & Korolev, A. (2015). Phase transformations in an ascending adiabatic mixed-phase cloud volume. *Journal of Geophysical Research: Atmospheres*, *120*(8), 3329–3353. https://doi.org/10.1002/2015JD023094

Pinsky, M., Khain, A., & Korolev, A. (2018). Theoretical analysis of liquid-ice interaction in the unsaturated environment with application to the problem of homogeneous mixing. *Journal of the Atmospheric Sciences*, *75*(4), 1045–1062. https://doi.org/10.1175/JAS-D-17-0228.1

Rogers, R. R., & Yau, M. K. (1996). *A short course in cloud physics*. Elsevier. Retrieved from https://www.elsevier.com/books/a-short-course-in-cloud-physics/yau/978-0-08-057094-5

Romps, D. M. (2010). A direct measure of entrainment. *Journal of the Atmospheric Sciences*, *67*(6), 1908–1927. https://doi.org/10.1175/2010JAS3371.1

Sanchez, K. J., Roberts, G. C., Diao, M., & Russell, L. M. (2020). Measured constraints on cloud top entrainment to reduce uncertainty of nonprecipitating stratocumulus shortwave radiative forcing in the Southern Ocean. *Geophysical Research Letters*, *47*(21), e2020GL090513. https://doi.org/10.1029/2020GL090513

Schima, J., McFarquhar, G., Romatschke, U., Vivekanandan, J., D'Alessandro, J., Haggerty, J., et al. (2022). Characterization of Southern Ocean boundary layer clouds using airborne radar, lidar, and in-situ cloud data: Results from SOCRATES. *Journal of Geophysical Research: Atmospheres*, *127*(21), e2022JD037277. https://doi.org/10.1029/2022jd037277

Shaw, R. A., Kostinski, A. B., & Larsen, M. L. (2002). Towards quantifying droplet clustering in clouds. *Quarterly Journal of the Royal Meteorological Society*, *128*(582), 1043–1057. https://doi.org/10.1256/003590002320373193

Shaw, R. A., Reade, W. C., Collins, L. R., & Verlinde, J. (1998). Preferential concentration of cloud droplets by turbulence: Effects on the early evolution of cumulus cloud droplet spectra. *Journal of the Atmospheric Sciences*, *55*(11), 1965–1976. https://doi.org/10.1175/1520-0469(1998)055<1965:PCOCDB>2.0.CO;2

Small, J. D., & Chuang, P. Y. (2008). New observations of precipitation initiation in warm cumulus clouds. *Journal of the Atmospheric Sciences*, *65*(9), 2972–2982. https://doi.org/10.1175/2008JAS2600.1

Sun, Z., & Shine, K. P. (1994). Studies of the radiative properties of ice and mixed-phase clouds. *Quarterly Journal of the Royal Meteorological Society*, *120*(515), 111–137. https://doi.org/10.1002/qj.49712051508

Tan, I., & Storelvmo, T. (2016). Sensitivity study on the influence of cloud microphysical parameters on mixed-phase cloud thermodynamic phase partitioning in CAM5. *Journal of the Atmospheric Sciences*, *73*(2), 709–728. https://doi.org/10.1175/JAS-D-15-0152.1

Tölle, M. H., & Krueger, S. K. (2014). Effects of entrainment and mixing on droplet size distributions in warm cumulus clouds. *Journal of Advances in Modeling Earth Systems*, *6*(2), 281–299. https://doi.org/10.1002/2012MS000209

UCAR/NCAR—Earth Observing Laboratory. (2018). NSF/NCAR GV HIAPER raw 2D-S imagery. Version 1.0 [Dataset]. UCAR/NCAREarth. https://doi.org/10.26023/8HMG-WQP3-XA0X

UCAR/NCAR—Earth Observing Laboratory. (2022). SOCRATES: Low rate (LRT - 1 sps) navigation, state parameter, and microphysics flight-level data. Version 1.4 [Dataset]. UCAR/NCAREarth. https://doi.org/10.5065/D6M32TM9

Wang, J., Jian, B., Wang, G., Zhao, Y., Li, Y., Letu, H., et al. (2021). Climatology of cloud phase, cloud radiative effects and precipitation properties over the Tibetan Plateau. *Remote Sensing*, *13*(3), 1–21. https://doi.org/10.3390/rs13030363

Wegener, A. (1911). *Thermodynamik der Atmosphäre*. J. A. Barth.

Wood, R. (2012). Stratocumulus clouds. *Monthly Weather Review*, *140*(8), 2373–2423. https://doi.org/10.1175/MWR-D-11-00121.1

Wu, W., & McFarquhar, G. M. (2019). NSF/NCAR GV Hiaper fast 2DS particle size distribution (psd) product data. Version 1.1 [Dataset]. UCAR/NCAR-Earth Observing Laboratory. https://doi.org/10.26023/8hmg-wqp3-xa0x

Yang, C. A., Diao, M., Gettelman, A., Zhang, K., Sun, J., McFarquhar, G., & Wu, W. (2021). Ice and supercooled liquid water distributions over the Southern Ocean based on in situ observations and climate model simulations. *Journal of Geophysical Research: Atmospheres*, *126*(24), e2021JD036045. https://doi.org/10.1029/2021JD036045

Yum, S. S., Wang, J., Liu, Y., Senum, G., Springston, S., McGraw, R., & Yeom, J. M. (2015). Cloud microphysical relationships and their implication on entrainment and mixing mechanism for the stratocumulus clouds measured during the VOCALS project. *Journal of Geophysical Research: Atmospheres*, *120*(10), 5047–5069. https://doi.org/10.1002/2014JD022802

Zondlo, M. A., Paige, M. E., Massick, S. M., & Silver, J. A. (2010). Vertical cavity laser hygrometer for the National Science Foundation Gulfstream-V aircraft. *Journal of Geophysical Research*, *115*(D20), D20309. https://doi.org/10.1029/2010JD014445